A&A, 707, A228 (2026)
https://doi.org/10.1051/0004-6361/202556177

Astronomy & Astrophysics

Euclid preparation

LXXVIII. Full-shape modelling of two-point and three-point correlation functions in real space

Euclid Collaboration: M. Guidi[1,2,⋆], A. Veropalumbo[3,4,5], A. Pugno[6], M. Moresco[1,2], E. Sefusatti[7,8,9], C. Porciani[6], E. Branchini[5,4,3], M.-A. Breton[10,11,12], B. Camacho Quevedo[8,13,7,14,10], M. Crocce[10,14], S. de la Torre[15], V. Desjacques[16], A. Eggemeier[6], A. Farina[5,3,4], M. Kärcher[15,17,18], D. Linde[19], M. Marinucci[20,21], A. Moradinezhad Dizgah[22], C. Moretti[13,23,7,8,9], K. Pardede[19], A. Pezzotta[24,25], E. Sarpa[13,23,9], A. Amara[26], S. Andreon[3], N. Auricchio[2], C. Baccigalupi[8,7,9,13], D. Bagot[27], M. Baldi[1,2,28], S. Bardelli[2], P. Battaglia[2], A. Biviano[7,8], M. Brescia[29,30], S. Camera[31,32,33], G. Cañas-Herrera[34,35,36], V. Capobianco[33], C. Carbone[37], V. F. Cardone[38,39], J. Carretero[40,41], M. Castellano[38], G. Castignani[2], S. Cavuoti[30,42], K. C. Chambers[43], A. Cimatti[44], C. Colodro-Conde[45], G. Congedo[46], L. Conversi[47,48], Y. Copin[49], F. Courbin[50,51], H. M. Courtois[52], A. Da Silva[53,54], H. Degaudenzi[55], G. De Lucia[7], H. Dole[56], M. Douspis[56], F. Dubath[55], X. Dupac[48], S. Dusini[21], S. Escoffier[57], M. Farina[58], R. Farinelli[2], F. Faustini[38,59], S. Ferriol[49], F. Finelli[2,60], P. Fosalba[14,10], S. Fotopoulou[61], M. Frailis[7], E. Franceschi[2], M. Fumana[37], S. Galeotta[7], B. Gillis[46], C. Giocoli[2,28], J. Gracia-Carpio[25], A. Grazian[62], F. Grupp[25,63], L. Guzzo[18,3,64], S. V. H. Haugan[65], W. Holmes[66], F. Hormuth[67], A. Hornstrup[68,69], K. Jahnke[70], M. Jhabvala[71], B. Joachimi[72], E. Keihänen[73], S. Kermiche[57], A. Kiessling[66], B. Kubik[49], M. Kümmel[63], M. Kunz[74], H. Kurki-Suonio[75,76], A. M. C. Le Brun[77], S. Ligori[33], P. B. Lilje[65], V. Lindholm[75,76], I. Lloro[78], G. Mainetti[79], D. Maino[18,37,64], E. Maiorano[2], O. Mansutti[7], S. Marcin[80], O. Marggraf[6], K. Markovic[66], M. Martinelli[38,39], N. Martinet[15], F. Marulli[1,2,28], R. Massey[81], E. Medinaceli[2], S. Mei[82,83], M. Melchior[84], Y. Mellier[85,86], M. Meneghetti[2,28], E. Merlin[38], G. Meylan[87], A. Mora[88], B. Morin[12], L. Moscardini[1,2,28], E. Munari[1,8], C. Neissner[89,41], S.-M. Niemi[34], C. Padilla[89], S. Paltani[55], F. Pasian[7], K. Pedersen[90], W. J. Percival[91,92,93], V. Pettorino[34], S. Pires[12], G. Polenta[59], M. Poncet[27], L. A. Popa[94], F. Raison[25], R. Rebolo[45,95,96], A. Renzi[20,21], J. Rhodes[66], G. Riccio[30], E. Romelli[7], M. Roncarelli[2], R. Saglia[63,25], Z. Sakr[97,98,99], A. G. Sánchez[25], D. Sapone[100], B. Sartoris[63,7], J. A. Schewtschenko[46], P. Schneider[5], T. Schrabback[101], M. Scodeggio[37], A. Secroun[57], G. Seidel[70], M. Seiffert[66], S. Serrano[14,102,10], P. Simon[6], C. Sirignano[20,21], G. Sirri[28], A. Spurio Mancini[103], L. Stanco[21], J. Steinwagner[25], P. Tallada-Crespí[40,41], D. Tavagnacco[7], A. N. Taylor[46], I. Tereno[53,104], N. Tessore[72], S. Toft[105,106], R. Toledo-Moreo[107], F. Torradeflot[41,40], A. Tsyganov[108], I. Tutusaus[98], L. Valenziano[2,60], J. Valiviita[75,76], T. Vassallo[63,7], G. Verdoes Kleijn[109], Y. Wang[110], J. Weller[63,25], G. Zamorani[2], F. M. Zerbi[3], E. Zucca[2], V. Allevato[30], M. Ballardini[111,112,2], M. Bolzonella[2], E. Bozzo[55], C. Burigana[113,60], R. Cabanac[98], M. Calabrese[114,37], A. Cappi[2,115], D. Di Ferdinando[28], J. A. Escartin Vigo[25], L. Gabarra[116], J. Martín-Fleitas[117], S. Matthew[46], M. Maturi[99,118], N. Mauri[44,28], R. B. Metcalf[1,2], A. A. Nucita[119,120,121], M. Pöntinen[75], I. Risso[122], V. Scottez[85,123], M. Sereno[2,28], M. Tenti[28], M. Viel[8,7,13,9,23], M. Wiesmann[65], Y. Akrami[124,125], I. T. Andika[126,127], S. Anselmi[21,20,11], M. Archidiacono[18,64], F. Atrio-Barandela[128], A. Balaguera-Antolinez[45,129], D. Bertacca[20,62,21], M. Bethermin[130], L. Blot[131,77], H. Böhringer[25,132,133], S. Borgani[134,8,7,9,23], M. L. Brown[135], S. Bruton[136], A. Calabro[38], F. Caro[38], C. S. Carvalho[104], T. Castro[7,9,8,23], F. Cogato[1,2], S. Conseil[49], S. Contarini[25], A. R. Cooray[137], O. Cucciati[2], S. Davini[4], F. De Paolis[119,120,121], G. Desprez[109], A. Díaz-Sánchez[138], J. J. Diaz[45], S. Di Domizio[5,4], J. M. Diego[139], P. Dimauro[38,140], A. Enia[1,2], Y. Fang[63], A. G. Ferrari[28], P. G. Ferreira[116], A. Finoguenov[75], A. Franco[120,119,121], K. Ganga[82], J. García-Bellido[124], T. Gasparetto[7], V. Gautard[141], E. Gaztanaga[10,14,142], F. Giacomini[28], F. Gianotti[2], G. Gozaliasl[143,75], C. M. Gutierrez[144], C. Hernández-Monteagudo[96,45], H. Hildebrandt[145], J. Hjorth[90], S. Joudaki[40], J. J. E. Kajava[146,147], Y. Kang[55], V. Kansal[148,149], D. Karagiannis[111,150], K. Kiiveri[73], C. C. Kirkpatrick[73], S. Kruk[48], M. Lattanzi[112],

⋆ Corresponding author: massimo.guidi6@unibo.it

L. Legrand[151,152], M. Lembo[86,112], F. Lepori[153], G. Leroy[154,81], G. F. Lesci[1,2], J. Lesgourgues[155], L. Leuzzi[2], T. I. Liaudat[156], A. Loureiro[157,158], J. Macias-Perez[159], G. Maggio[7], M. Magliocchetti[58], F. Mannucci[160], R. Maoli[161,38], C. J. A. P. Martins[162,163], L. Maurin[56], M. Miluzio[48,164], P. Monaco[134,7,9,8], G. Morgante[2], S. Nadathur[142], K. Naidoo[142], A. Navarro-Alsina[6], S. Nesseris[124], L. Pagano[111,112], F. Passalacqua[20,21], K. Paterson[70], L. Patrizii[28], A. Pisani[57], D. Potter[153], S. Quai[1,2], M. Radovich[62], P. Reimberg[85], P.-F. Rocci[56], G. Rodighiero[20,62], S. Sacquegna[119,120,121], M. Sahlén[165], D. B. Sanders[43], A. Schneider[153], D. Sciotti[38,39], E. Sellentin[166,36], L. C. Smith[167], J. G. Sorce[168,56], K. Tanidis[116], C. Tao[57], G. Testera[4], R. Teyssier[169], S. Tosi[5,4,3], A. Troja[20,21], M. Tucci[55], C. Valieri[28], A. Venhola[170], D. Vergani[2], F. Vernizzi[171], G. Verza[172], P. Vielzeuf[57], and N. A. Walton[167]

(Affiliations can be found after the references)

Received 30 June 2025 / Accepted 21 October 2025

ABSTRACT

We investigated the accuracy and range of validity of the perturbative model for the two-point (2PCF) and three-point (3PCF) correlation functions in real space in view of the forthcoming analysis of the *Euclid* mission spectroscopic sample. We took advantage of clustering measurements from four snapshots of the Flagship I N-body simulations at $z = \{0.9, 1.2, 1.5, 1.8\}$, which mimic the expected galaxy population in the ideal case, i.e. in the absence of observational effects such as purity and completeness. For the 3PCF we considered all available triangular configurations given a minimal separation ($r_{\rm min}$). We first assessed the model performance by fixing the cosmological parameters and evaluating the goodness of fit provided by the perturbative bias expansion in the joint analysis of the two statistics, finding an overall agreement with the data down to separations of $20\,h^{-1}$ Mpc. Subsequently, we built on the state-of-the-art analysis and extended it to include the dependence on three cosmological parameters: the amplitude of scalar perturbations ($A_{\rm s}$), the matter density ($\omega_{\rm cdm}$), and the Hubble parameter (h). To achieve this goal, we developed an emulator capable of generating fast and robust modelling predictions for the two summary statistics, which thus enables an efficient sampling of the joint likelihood function. We therefore present the first joint full-shape analysis of the real-space 2PCF and 3PCF, testing the consistency and constraining power of the perturbative model across both probes and assessing its performance in a combined likelihood framework. We explored possible systematic uncertainties induced by the perturbative model at small scales, finding an optimal scale cut of $r_{\rm min} = 30\,h^{-1}$ Mpc for the 3PCF when imposing an additional limitation on the nearly isosceles triangular configurations included in the data vector. This work is part of a series of papers in which we validate theoretical models for galaxy clustering measurements in preparation for the *Euclid* mission.

Key words. large-scale structure of Universe

1. Introduction

The *Euclid* mission (Laureijs et al. 2011) is, along with the Dark Energy Spectroscopic Instrument (DESI; DESI Collaboration 2016), *Vera Rubin* Observatory (Ivezic et al. 2009), and *Nancy Grace Roman* Telescope initiatives (Dore et al. 2019), a stage IV (Albrecht et al. 2006) observational campaign expected to significantly advance our understanding of the Universe by mapping cosmological perturbations on an unprecedented volume. *Euclid* will combine two major probes of the large-scale structure: galaxy clustering and weak lensing. The scientific potential of this combination, along with a description of the instrumentation that will enable it, is described in the recent overview paper Euclid Collaboration: Mellier et al. (2025). The spectroscopic galaxy sample, in particular, will cover the redshift range $0.9 \leq z \leq 1.8$, collecting redshift measurements for millions of Hα-emitting galaxies across a total area of 14 000 deg^2.

Galaxy clustering exploits the statistical properties of the fluctuations in the galaxy distribution at large scales, measuring and analysing, in the standard approach, its correlation functions, starting with the two-point correlation function (2PCF) or its Fourier-space counterpart, the power spectrum. A major contribution to cosmological studies over the past two decades came from using the baryonic acoustic oscillations (BAOs) present in the 2PCF as a standard ruler to reconstruct the background expansion (Seo & Eisenstein 2003; Eisenstein et al. 2005; Percival et al. 2007; Wang et al. 2017; Zhao et al. 2017; Adame et al. 2025). Additional constraints come from the anisotropy induced on two-point correlators by redshift-space distortions (Peacock et al. 2001; Guzzo et al. 2008; Beutler et al. 2017; Grieb et al. 2017; Pezzotta et al. 2017; Hou et al. 2018) and, more generally, from the full-shape analysis of their redshift-space multipoles, with the aim of extracting all available information from the clustering measurements (Sánchez et al. 2013, 2017; D'Amico et al. 2020; Ivanov et al. 2020; Tröster et al. 2020; Adame et al. 2025).

In recent years, the inclusion in galaxy clustering analyses of higher-order correlation functions – such as the three-point correlation function (3PCF) and, in Fourier space, the bispectrum – has become increasingly standard. These statistics quantify the non-Gaussian properties of the galaxy distribution as a random field. Different sources of non-Gaussianity are directly related to non-linearities in the evolution of matter perturbations (Fry 1984), galaxy bias (Fry & Gaztañaga 1993; Fry 1994; Frieman & Gaztanaga 1994), and redshift-space distortions (Hivon et al. 1995; Scoccimarro et al. 1999), or possibly to a primordial non-Gaussian component due to inflationary physics (Verde et al. 2000; Scoccimarro 2000; Scoccimarro et al. 2004). The joint analysis of the galaxy power spectrum and bispectrum has been performed over the last few years in several studies involving Baryon Oscillations Spectroscopic Survey (BOSS) datasets (Dawson et al. 2013) datasets, leading to improvements in constraints on cosmological parameters in the context of the standard model and its extensions (see e.g. Gil-Marín et al. 2017; D'Amico et al. 2020; Philcox & Ivanov 2022) and better constraints on initial conditions (D'Amico et al. 2025; Cabass et al. 2022).

The full exploitation of the information provided by the 3PCF in configuration space, despite its clear advantages over the bispectrum in terms of accounting for survey geometry effects, has long been hampered by the computational cost of its estimation in large datasets. Early studies focused on a subset of all potentially measurable configurations, focusing on the galaxy properties and non-linear bias (Jing & Börner

2004; Gaztañaga et al. 2005; McBride et al. 2011; Marín 2011; Marín et al. 2013; Moresco et al. 2017) and the detection of acoustic features (Gaztañaga et al. 2009; Moresco et al. 2021). The introduction of an estimator based on a spherical harmonic expansion (Slepian & Eisenstein 2015, 2018) has substantially reduced the computational burden, enabling a full exploitation of the information potentially encoded in the 3PCF (Slepian et al. 2017, 2018).

Yet, in a likelihood analysis, an additional disadvantage of the 3PCF compared to the bispectrum is still present at the level of the evaluation of the theoretical model. Predictions for configuration-space statistics are typically obtained from a first evaluation of their Fourier-space counterpart. For the 2PCF, this mapping is efficiently handled using the FFTLog algorithm (Hamilton 2000) in one dimension. In the case of the 3PCF, while some works applied the 1D fast Fourier transform (FFT) to leading-order (LO) perturbative predictions (Slepian & Eisenstein 2017; Sugiyama et al. 2021; Veropalumbo et al. 2022), more general methods instead adopted a 2D FFT (Fang et al. 2020) to transform any bispectrum model, when expanded into spherical harmonics, into its configuration-space equivalent (Umeh 2021; Guidi et al. 2023; Farina et al. 2026; Pugno et al. 2025).

Cosmological perturbation theory (PT) plays a crucial role in our understanding of galaxy clustering at large scales (see Bernardeau et al. 2002, for a classical review). Significant effort has been made in the past decade to identify all potential effects that could lead to biased estimates of cosmological parameters if ignored. This includes the impact of small-scale matter fluctuations on large-scale clustering; this motivated the development of the effective field theory of large-scale structure (EFTofLSS; Baumann et al. 2012; Carrasco et al. 2012), non-local (Chan et al. 2012; Baldauf et al. 2012), re-normalised (McDonald 2006; McDonald & Roy 2009; Assassi et al. 2014; Eggemeier et al. 2019), higher derivative bias (Bardeen et al. 1986; Fujita et al. 2020), and infrared re-summation (Blas et al. 2016b). Here we set aside, for the sake of brevity, redshift-space distortion effects, which are extremely important in actual data analysis but not relevant for this work. The state-of-the-art model, which is a perturbative prediction at the next-to-leading order (NLO) for the power spectrum and at the LO for the bispectrum, is at the basis of current full-shape analyses of the galaxy power spectrum, bispectrum, and 2PCF. A full-shape analysis involving the 3PCF (on equal footing) is still lacking due to the computational burden of its numerical evaluation.

This work is part of a series of papers in preparation for the *Euclid* mission. The series provides an extensive validation of analytical and, in some cases, numerical models for galaxy clustering statistics. Paper I focused on the real-space power spectrum (Euclid Collaboration: Pezzotta et al. 2024).

Here we instead explore the range of validity of perturbative models in describing real-space measurements of the 2PCF and 3PCF in synthetic catalogues that reproduce the density and clustering amplitude expected for the *Euclid* spectroscopic sample. In addition, we apply such models to a full-shape joint analysis of the two statistics. To do so, we developed an emulator for both 2PCF and 3PCF predictions as a function of three cosmological parameters, the amplitude of scalar perturbations (A_s), the cold dark matter (CDM) density parameter ($\omega_{\rm cdm}$), and the reduced Hubble parameter (h). This constitutes an important step towards a complete, configuration-space analysis of galaxy clustering datasets in general and towards the goals of the *Euclid* mission more specifically.

This paper is organised as follows. In Sects. 2 and 3 we introduce the basic definitions of Fourier-space and configuration-space correlators along with a brief overview of their theoretical model in PT. Section 4 presents the synthetic galaxy catalogues and the simulation on which they are based, the 2PCF and 3PCF measurements, and the theoretical model for the relative covariance matrices. In Sect. 5 we describe the fitting procedure and the performance metrics employed to assess model accuracy and precision. Our results are presented in Sects. 6 and 7: we first fix the cosmological parameters to assess the goodness of fit (GoF) of the model and then explore the full-shape analysis of 2PCF and 3PCF in order to constrain the same parameters. Lastly, in Sect. 8 we present our conclusions. In Appendix B we include a more detailed description of the 2PCF and 3PCF emulator and its validation.

2. Definitions and conventions

For convenience, we use the following notation to refer to the integration over the infinite volume of a loop variable, $\mathbf{q}$,

$$\int_{\mathbf{q}} := \int \frac{\mathrm{d}^3 q}{(2\pi)^3}, \tag{1}$$

and we also adopt the following convention for the Fourier transform and its inverse

$$\delta(\mathbf{k}) := (2\pi)^3 \int_{\mathbf{q}} \delta(\mathbf{q})\, \mathrm{e}^{\mathrm{i}\mathbf{k}\cdot\mathbf{q}}, \tag{2}$$

$$\delta(\mathbf{x}) := \int_{\mathbf{k}} \delta(\mathbf{k})\, \mathrm{e}^{-\mathrm{i}\mathbf{k}\cdot\mathbf{x}}. \tag{3}$$

Under the assumption of statistical homogeneity and isotropy, the power spectrum $P(k)$ of a generic density contrast $\delta(\mathbf{k})$ is therefore defined as

$$\langle \delta(\mathbf{k}_1)\, \delta(\mathbf{k}_2) \rangle := (2\pi)^3 \delta_{\rm D}(\mathbf{k}_1 + \mathbf{k}_2)\, P(k), \tag{4}$$

where $k := |\mathbf{k}_1|$. The corresponding two-point function $\xi(r) := \langle \delta(\mathbf{x}) \delta(\mathbf{x} + \mathbf{r}) \rangle$, where $r := |\mathbf{r}|$, can be obtained as its Fourier transform, is

$$\xi(r) = \int_{\mathbf{k}} P(k)\, \mathrm{e}^{\mathrm{i}\mathbf{k}\cdot\mathbf{r}} = \int \frac{\mathrm{d}k}{2\pi^2} k^2\, j_0(kr)\, P(k), \tag{5}$$

where j_n represent the spherical Bessel functions of n-th order. Similarly, the bispectrum $B(\mathbf{k}_1, \mathbf{k}_2, \mathbf{k}_3)$, i.e. the 3PCF of the Fourier-space density contrast $\delta(\mathbf{k})$, is defined as

$$\langle \delta(\mathbf{k}_1) \delta(\mathbf{k}_2) \delta(\mathbf{k}_3) \rangle := (2\pi)^3\, \delta_{\rm D}(\mathbf{k}_1 + \mathbf{k}_2 + \mathbf{k}_3)\, B(k_1, k_2, k_3). \tag{6}$$

Here the Dirac delta distribution forces the three wave vectors $\{\mathbf{k}_1, \mathbf{k}_2, \mathbf{k}_3\}$ to form a closed triangle, so that k_3 can be written as a function of k_1, k_2 and the cosine of the angle between $\mathbf{k}_1$ and $\mathbf{k}_2$, denoted as $\mu_{12} := \mathbf{k}_1 \cdot \mathbf{k}_2 / k_1 k_2$. We can therefore consider an expansion with such an angle dependence in Legendre polynomials,

$$B(k_1, k_2, k_3) = \sum_\ell B_\ell(k_1, k_2)\, \mathcal{L}_\ell(\mu_{12}), \tag{7}$$

with coefficients defined as

$$B_\ell(k_1, k_2) = \frac{2\ell + 1}{2} \int_{-1}^{1} \mathrm{d}\mu_{12}\, B(k_1, k_2, k_3)\, \mathcal{L}_\ell(\mu_{12}). \tag{8}$$

The 3PCF, in configuration space, is defined, adopting the notation $\mathbf{r}_{ij} := \mathbf{r}_i - \mathbf{r}_j$, as

$$\zeta(r_{12}, r_{13}, r_{23}) := \langle \delta(\mathbf{r}_1)\, \delta(\mathbf{r}_2)\, \delta(\mathbf{r}_3) \rangle, \tag{9}$$

and, in the same way, the dependence on the angle between $\mathbf{r}_{12}$ and $\mathbf{r}_{13}$ can be expanded in Legendre polynomials as

$$\zeta(r_{12}, r_{13}, r_{23}) = \sum_\ell \zeta_\ell(r_{12}, r_{13}) \mathcal{L}_\ell(\mu_{12,13}), \tag{10}$$

where now we define the cosine $\mu_{12,13} := \mathbf{r}_{12} \cdot \mathbf{r}_{13}/(r_{12} r_{13})$ and the coefficients are given by

$$\zeta_\ell(r_{12}, r_{13}) := \frac{2\ell + 1}{2} \int_{-1}^{1} \mathrm{d}\mu_{12,13}\, \zeta(r_{12}, r_{13}, r_{23})\, \mathcal{L}_\ell(\mu_{12,13}). \tag{11}$$

The relation between the 3PCF and the bispectrum can be expressed in terms of their respective multipoles B_ℓ and ζ_ℓ as

$$\zeta_\ell(r_{12}, r_{13}) = (-1)^\ell \int \frac{\mathrm{d}k_1\, \mathrm{d}k_2}{(2\pi)^6} B_\ell(k_1, k_2)\, j_\ell(k_1 r_{12})\, j_\ell(k_2 r_{13}). \tag{12}$$

As we will see, the expansion in multipoles will be crucial to defining an efficient estimator for the 3PCF and for a fast evaluation of its theoretical prediction.

3. Theoretical models

This section provides a brief introduction to the real-space modelling of the 2PCF and 3PCF in cosmological PT (Bernardeau et al. 2002). We considered specifically a one-loop expression for the 2PCF accounting for a general bias expansion (Desjacques et al. 2018), corresponding to the EFTofLSS expression described in a companion paper (Euclid Collaboration: Kärcher et al., in prep.), to which we refer the reader for further details. The prediction for the 3PCF is instead at tree level in PT.

3.1. Eulerian perturbation theory and galaxy bias

In Eulerian PT, the equations describing the evolution of the matter density and velocity field, which are continuity and Euler equations, are solved perturbatively assuming the density contrast $\delta(\mathbf{x})$ to be small at large scales. The non-linear solution is given by the sum of the solution to the linearised equations plus higher-order corrections.

In addition, the relation between the galaxy density contrast $\delta_\mathrm{g}(\mathbf{x})$ and the matter field $\delta(\mathbf{x})$ is also given in terms of a perturbative expansion. The terms relevant for the one-loop power spectrum and 2PCF models are given by

$$\begin{aligned}\delta_\mathrm{g}(\mathbf{x}) = b_1\, \delta(\mathbf{x}) + \frac{b_2}{2}\delta^2(\mathbf{x}) + b_{\nabla^2}\nabla^2\delta(\mathbf{x}) \\ + b_{\mathcal{G}_2}\mathcal{G}_2\,(\Phi_\mathrm{v}\,|\,\mathbf{x}) + b_{\Gamma_3}\Gamma_3(\mathbf{x}),\end{aligned} \tag{13}$$

where $\mathcal{G}_2$ and Γ_3 are non-local operators, defined as

$$\mathcal{G}_2(\Phi|\mathbf{x}) := [\partial_i\partial_j\Phi(\mathbf{x})]^2 - [\partial^2\Phi(\mathbf{x})]^2, \tag{14}$$

$$\Gamma_3(\mathbf{x}) := \mathcal{G}_2(\Phi|\mathbf{x}) - \mathcal{G}_2(\Phi_v|\mathbf{x}), \tag{15}$$

and $\Phi(\mathbf{x})$ and $\Phi_v(\mathbf{v})$ represent the gravitational and velocity potential. The bias relation in Eq. (13) consists of all operators built from second derivatives of the gravitational and velocity potential. It includes the linear (b_1) and quadratic (b_2), local bias contributions (Kaiser 1984; Szalay 1988; Coles et al. 1993; Fry & Gaztañaga 1993), omitting the cubic local operator that leads to a correction that can be absorbed in a renormalised linear bias parameter (Szalay 1988; McDonald 2006; McDonald & Roy 2009; Assassi et al. 2014; Eggemeier et al. 2019). It also includes non-local contributions ($b_{\mathcal{G}_2}, b_{\Gamma_3}$) induced by non-linear evolution (Catelan et al. 1998; Chan et al. 2012; Baldauf et al. 2012) and higher derivative correction to linear bias (b_{∇^2}; Bardeen et al. 1986; Desjacques 2008; Fujita et al. 2020). For a detailed review, see Desjacques et al. (2018).

The most general and conservative assumption in fitting the galaxy correlation models to their measurements consist in considering all bias parameters as free, independent parameters to be determined by the data along with the cosmological parameters. On the other hand, we do know that the bias parameters are correlated, and large portions of the parameter space are in fact non-physical. We can take advantage of specific relations among the bias parameters to reduce the number of nuisance parameters. We considered two such relations. The first, given by

$$b_{\mathcal{G}_2}^{\mathrm{ex-set}} = 0.524 - 0.547\, b_1 + 0.046\, b_1^2, \tag{16}$$

is a quadratic fit obtained by Eggemeier et al. (2020) to the excursion-set prediction of Sheth et al. (2013). The second relation, given instead by

$$b_{\Gamma_3}^{\mathrm{coev}} = -\frac{1}{6}(b_1 - 1) - \frac{5}{2} b_{\mathcal{G}_2} + b_{\Gamma_3}^{\mathcal{L}}, \tag{17}$$

is derived in Eggemeier et al. (2019) assuming the evolution of conserved galaxy number density (hence, 'coevolution') after formation, with the subscript $\mathcal{L}$ indicates the corresponding Lagrangian quantities at the formation moment.

The resulting, perturbative expression for the galaxy power spectrum in real space, $P_\mathrm{g}(k)$, omitting stochastic contributions irrelevant for the 2PCF prediction, then reads

$$P_\mathrm{g}(k) = P_\mathrm{g}^{\mathrm{tree}}(k) + P_\mathrm{g}^{1-\mathrm{loop}}(k) + P_\mathrm{g}^{\mathrm{ctr}}(k). \tag{18}$$

The linear, tree level, leading term is simply proportional to the linear matter power spectrum,

$$P_\mathrm{g}^{\mathrm{tree}}(k) = b_1^2\, P_\mathrm{L}(k), \tag{19}$$

while the one-loop correction in standard PT is

$$\begin{aligned}P_\mathrm{g}^{1-\mathrm{loop}}(k) &= P_{\mathrm{g},22}(k) + P_{\mathrm{g},13}(k) \\ &= 2\int_\mathbf{q} K_2^2\,(\mathbf{q}, \mathbf{k}-\mathbf{q})\; P_\mathrm{L}\,(|\mathbf{k}-\mathbf{q}|)\; P_\mathrm{L}(q)\end{aligned} \tag{20}$$

$$+ 6\, b_1\, P_\mathrm{L}(k) \int_\mathbf{q} K_3\,(\mathbf{q}, -\mathbf{q}, \mathbf{k})\; P_\mathrm{L}(q), \tag{21}$$

where the kernels describing non-linear matter density evolution and non-linear bias are

$$K_2(\mathbf{k}_1, \mathbf{k}_2) = b_1 F_2(\mathbf{k}_1, \mathbf{k}_2) + \frac{1}{2}\, b_2 + b_{\mathcal{G}_2} S(\mathbf{k}_1, \mathbf{k}_2), \tag{22}$$

$$\begin{aligned}K_3(\mathbf{k}_1, \mathbf{k}_2, \mathbf{k}_3) = b_1 F_3(\mathbf{k}_1, \mathbf{k}_2, \mathbf{k}_3) + b_2 F_2(\mathbf{k}_1, \mathbf{k}_2) \\ + 2 b_{\mathcal{G}_2}\, S\,(\mathbf{k}_1, \mathbf{k}_{12})\, F_2(\mathbf{k}_2, \mathbf{k}_3) \\ + 2 b_{\Gamma_3}\, S\,(\mathbf{k}_1, \mathbf{k}_{12})\, [F_2(\mathbf{k}_2, \mathbf{k}_3) - G_2(\mathbf{k}_2, \mathbf{k}_3)],\end{aligned} \tag{23}$$

with

$$S\,(\mathbf{k}_1, \mathbf{k}_2) = \frac{(\mathbf{k}_1 \cdot \mathbf{k}_2)^2}{k_1^2 k_2^2} - 1, \tag{24}$$

$$F_2(\mathbf{k}_1, \mathbf{k}_2) = \frac{5}{7} + \frac{1}{2}\frac{\mathbf{k}_1 \cdot \mathbf{k}_2}{k_1 k_2}\left(\frac{k_2}{k_1} + \frac{k_1}{k_2}\right) + \frac{2}{7}\frac{(\mathbf{k}_1 \cdot \mathbf{k}_2)^2}{k_1^2 k_2^2}, \tag{25}$$

$$G_2(\mathbf{k}_1, \mathbf{k}_2) = \frac{3}{7} + \frac{1}{2}\frac{\mathbf{k}_1 \cdot \mathbf{k}_2}{k_1 k_2}\left(\frac{k_2}{k_1} + \frac{k_1}{k_2}\right) + \frac{4}{7}\frac{(\mathbf{k}_1 \cdot \mathbf{k}_2)^2}{k_1^2 k_2^2}. \tag{26}$$

The last term in the power spectrum model accounts for the fully degenerate contributions from the effective field theory (EFT) matter counter-terms depending on the effective speed of sound, c_s (Baumann et al. 2012; Carrasco et al. 2012) and the higher derivative correction to linear bias,

$$P_{\rm g}^{\rm ctr}(k) = -2\,b_1\left(b_1\,c_{\rm s}^2 + b_{\nabla^2\delta}\right)k^2\,P_{\rm L}(k) \tag{27}$$

$$:= -2\,c_0\,k^2\,P_{\rm L}(k), \tag{28}$$

with the parameter $c_0 := b_1 c_s^2 + b_{\nabla^2\delta}$. Finally, the expression for the galaxy bispectrum at tree-level in PT is simply

$$B_{\rm g}^{\rm tree}(k_1,k_2,k_3) = 2b_1^2\,K_2(\mathbf{k}_1,\mathbf{k}_2)\,P_{\rm L}(k_1)\,P_{\rm L}(k_2) + \text{cyc.}, \tag{29}$$

where, again, we neglect shot-noise contributions.

3.2. Infrared re-summation

The expressions described above do not account for the additional smearing of the baryonic features due to non-linear evolution (Eisenstein et al. 2007; Smith et al. 2007; Crocce & Scoccimarro 2008; Matsubara 2008; Desjacques et al. 2010; Baldauf et al. 2015; Senatore & Zaldarriaga 2015). We modeled this effect in the power spectrum following the approach of Blas et al. (2016a) in terms of a wiggle-no wiggle splitting of the linear power spectrum,

$$P_{\rm L}(k) = P_{\rm nw}(k) + P_{\rm w}(k), \tag{30}$$

obtained adopting the specific procedure of Vlah et al. (2016) (see Appendix C in Euclid Collaboration: Pezzotta et al. 2024, for a detailed description).

The linear galaxy power spectrum in real space is then replaced by a LO contribution,

$$P_{\rm g}^{\rm IR,\,LO}(k) = b_1^2\left[P_{\rm nw}(k) + {\rm e}^{-k^2\Sigma^2}P_{\rm w}(k)\right], \tag{31}$$

with the constant Σ^2 representing the anisotropic variance of the relative displacement field (Eisenstein et al. 2007),

$$\Sigma^2 = \frac{1}{6\pi^2}\int_0^{k_S}{\rm d}q\,P_{\rm nw}(q)\left[1 - j_0\left(\frac{q}{k_{\rm osc}}\right) + 2\,j_2\left(\frac{q}{k_{\rm osc}}\right)\right], \tag{32}$$

where $k_{\rm osc} = 1/\ell_{\rm osc}$ is the wavenumber associated with the BAOs scale $\ell_{\rm osc} = 110\,h^{-1}\,{\rm Mpc}$, while $k_S = 0.2\,h\,{\rm Mpc}^{-1}$ is an upper limit of integration whose specific choice does not lead to significant differences on the final result. To give an idea, for the redshift values considered in this work, $z \in \{0.9, 1.2, 1.5, 1.8\}$, we obtain $\Sigma \in \{8.72, 6.82, 5.22, 4.34\}$.

The one-loop prediction is now included in the NLO correction as

$$P_{\rm g}^{\rm IR,\,LO+NLO}(k) = b_1^2\,P_{\rm g,\,nw}(k) + \left(1 + k^2\Sigma^2\right){\rm e}^{-k^2\Sigma^2}\,b_1^2 P_{\rm w}(k) + P_{\rm g}^{\rm IR,\,1-loop}(k), \tag{33}$$

where the last term denotes the galaxy power spectrum one-loop correction evaluated in terms of the LO matter power spectrum, which is, schematically,

$$P_{\rm g,\,nw}^{\rm IR,\,1-loop}(k) := P_{\rm g}^{\rm 1-loop}\left[P_{\rm nw}(k) + {\rm e}^{-k^2\Sigma^2}P_{\rm w}(k)\right]. \tag{34}$$

The tree-level bispectrum expression is replaced instead by the LO prediction (Ivanov & Sibiryakov 2018)

$$B_{\rm g}^{\rm tree,LO}(k_1,k_2,k_3) = 2\,b_1^2\,K_2(\mathbf{k}_1,\mathbf{k}_2) \times \left[P_{\rm nw}(k_1)\,P_{\rm nw}(k_2) + {\rm e}^{-k_1^2\Sigma^2}\,P_{\rm w}(k_1)\,P_{\rm nw}(k_2) + {\rm e}^{-k_2^2\Sigma^2}\,P_{\rm w}(k_2)P_{\rm nw}(k_1)\right] + 2\ \text{perm.} \tag{35}$$

In what follows we retain, for clarity, the notation of Sect. 3.1 for all contributions to each correlation function, while we assume as implicit the implementation of infrared re-summation as described here.

3.3. Evaluation of 2PCF and 3PCF

The 2PCF was computed from the power spectrum of Eq. (18) according to the Hankel transform of Eq. (5), implemented using the `FFTLog` approach of Hamilton (2000). The decomposition in Legendre polynomials of the 3PCF defined in Eq. (10) allows us to apply an analogous procedure to this statistic. We can in fact consider the 2D extension of the `FFTLog` algorithm proposed by Fang et al. (2020) for an efficient evaluation of the integral in Eq. (12) over the $B_\ell(k_1,k_2)$ functions, (see Umeh 2021; Guidi et al. 2023; Farina et al. 2026; Pugno et al. 2025, for further details).

However, the implementation of the `2DFFTLog` approach still constitutes a computational burden when considered in the context of Monte Carlo sampling of a likelihood function over a large parameter space. For this reason, we developed an emulator for the 3PCF for a full set of cosmological and nuisance parameters. This allowed us to efficiently extend the full-shape analysis of the 2PCF to include the next, higher-order statistic. In fact, our emulator provides all contributions to the 2PCF and 3PCF where a combination of bias parameters can be factorised and describes the cosmological dependence of each term on the scalar amplitude parameter (A_s), the matter density ($\omega_{\rm cdm}$), and the Hubble parameter (h). A detailed description of the emulator, along with validation tests, can be found in Appendix B.

4. Data

We validated our theoretical model against a set of synthetic galaxy catalogues obtained from the Euclid Flagship I N-body simulation. The catalogues adopt a halo occupation distribution (HOD) prescription to describe the population of Hα galaxies expected for the *Euclid* spectroscopic sample. We provide below a concise description of the galaxy catalogues, referring the reader to Euclid Collaboration: Pezzotta et al. (2024) for further details.

4.1. Euclid simulation

The Flagship I simulation uses the `PKDGRAV3` code (Potter et al. 2017) to track the evolution of two trillion dark matter particles in a box of size $L = 3780\ h^{-1}$ Mpc, with a mass resolution, $m_{\rm p} \sim 2.398 \times 10^9\ h^{-1}\ M_\odot$. It assumes a flat, ΛCDM cosmology with the fiducial parameters given in Table 1[1].

We considered four comoving snapshots at redshift $z = 0.9$, 1.2, 1.5, and 1.8. In each snapshot, a friends-of-friends halo catalogue with a minimum mass corresponding to ten particles, is constructed. Galaxies are then assigned to these halos using a HOD prescription derived from the Flagship I light cone catalogue, designed to reproduce the Model 3 distribution of Pozzetti et al. (2016). Specifically, the HOD parameters are are chosen to match the expected selection function of the Euclid spectroscopic sample with a Hα flux limit of $f_{\rm H\alpha} > 2\times10^{-16}\,{\rm erg\,cm^{-2}\,s^{-1}}$, as outlined by Euclid Collaboration: Scaramella et al. (2022). Table 2 shows

[1] For the slight difference with respect to Potter et al. (2017), we refer the reader to the explanation in Euclid Collaboration: Pezzotta et al. (2024).

Table 1. Fiducial parameters of the flat ΛCDM model.

h	ω_b	ω_cdm	$10^9 \times A_s$	n_s	M_ν[eV]
0.67	0.0219961	0.121203	2.09427	0.97	0.0

Notes. The table lists, from left to right, h, ω_b, ω_cdm, A_s, n_s, and the total neutrino mass (M_ν).

Table 2. Key properties of the synthetic galaxy catalogues.

z	N_g	$\bar{n}_g\,[h^3\mathrm{Mpc}^{-3}]$	b_1
0.9	110 321 755	0.0020	1.4
1.2	55 563 490	0.0010	1.8
1.5	31 613 213	0.0006	2.0
1.8	16 926 864	0.0003	2.5

Notes. For each snapshot, the table lists the total number of galaxies (N_g), the number density ($\bar{n}_\mathrm{g}$), and the linear bias parameter (b_1) measured in Euclid Collaboration: Pezzotta et al. (2024) from the matter power spectrum.

for each snapshot the total number of galaxies, the number density and a value for the linear bias obtained from measurements of the galaxy and matter power spectra. For a more detailed description of the mock galaxy catalogue we refer the reader, again, to Euclid Collaboration: Pezzotta et al. (2024).

We fitted our model to measurements from the full simulation volume, which is approximately three to six times larger than the effective volume of the Euclid redshift bins assumed for the forecasts analysis of Euclid Collaboration: Blanchard et al. (2020). The large simulation volume enables a stringent test of the model, which ensures that any residual theory systematic error is well within the expected precision of future measurements.

The catalogue we used does not take into account observational systematic effects such as target incompleteness, sample purity, and the impact of the angular footprint or radial selection function. A comprehensive exploration of such effects is left to other works (see Euclid Collaboration: Monaco et al., (in prep.); Euclid Collaboration: Risso et al. 2026).

4.2. Clustering measurements

We estimated the 2PCF using the natural estimator (Peebles 1973):

$$\hat{\xi}(r) := \frac{N_\mathrm{DD}(r)}{N_\mathrm{RR}(r)} - 1, \tag{36}$$

where $N_\mathrm{DD}(r)$ and $N_\mathrm{RR}(r)$ represent the pair counts, as a function of separation r, in the data and a random distribution with, in this ideal case, constant density. This is equivalent to the usual Landy–Szalay estimator (Landy & Szalay 1993) in the case of a cubic box with periodic boundary conditions (they should both lead to the same variance). We took advantage of this property to also estimate analytically the number of pairs from the random catalogue as

$$N_\mathrm{RR}(r) = \frac{4\pi}{3}\bar{n}^2 V\left[\left(r+\frac{\Delta r}{2}\right)^3 - \left(r-\frac{\Delta r}{2}\right)^3\right], \tag{37}$$

where we assume a separation bin of size Δr centred on r, $\bar{n}$ being the mean galaxy number density and V the volume of the box.

We measured the 2PCF in the four snapshots for separations ranging from $r_\mathrm{min} = 0\,h^{-1}$ Mpc to $r_\mathrm{max} = 150\,h^{-1}$ Mpc. We used linearly spaced bins with a width of $\Delta r = 5\,h^{-1}$ Mpc. The results are displayed in the top panels of Fig. 1, where each column represents one of the four redshift snapshots. In the analysis presented in Sects. 6 and 7, we restricted the 2PCF data vector to separations $r \leq r_\mathrm{max} = 140\,h^{-1}$ Mpc.

The Landy–Szalay estimator for the 2PCF can be easily extended to the analogous estimator for the 3PCF, constructed in terms of triplet counts (see e.g. Szapudi & Szalay 1998). However, since such an estimator scales with the number of galaxies N_g as $O(N_g^3)$, its computational cost quickly becomes prohibitive when it comes to very large datasets such as those we considered here, where N_g is around 10^8. To resolve this issue, Slepian & Eisenstein (2015) introduced an estimator based on the spherical harmonics decomposition (SHD), which improves significantly the computational efficiency. In this approach, the dependence of the 3PCF on the angle between the triangle sides $\mathbf{r}_{12}$ and $\mathbf{r}_{13}$ is expanded in terms of Legendre polynomials according to Eq. (10). As a result, the full estimator $\hat{\zeta}(r_{12}, r_{13}, r_{23})$ is written as a function of an estimator $\hat{\zeta}_\ell(r_{12}, r_{13})$ of the expansion coefficients as

$$\hat{\zeta}(r_{12}, r_{13}, r_{23}) = \sum_{\ell=0}^{\ell_\mathrm{max}} \hat{\zeta}_\ell(r_{12}, r_{13})\,\mathcal{L}(\mu_{12,13}), \tag{38}$$

thereby reducing the computational complexity to $O(N_g^2)$. The coefficients are estimated as

$$\hat{\zeta}_\ell(r_{12}, r_{13}) = \frac{N_{\mathrm{DDD},\ell} - 3N_{\mathrm{DDR},\ell} + 3N_{\mathrm{DRR},\ell} - N_{\mathrm{RRR},\ell}}{N_{\mathrm{RRR},0}}, \tag{39}$$

where $N_{\mathrm{DDD},\ell}$, $N_{\mathrm{DDR},\ell}$, $N_{\mathrm{DRR},\ell}$, and $N_{\mathrm{DRR},\ell}$ are, in turn, the coefficients of the Legendre expansion of the triplets counts from the galaxy catalogue, from the random and the two mixed terms, directly evaluated in the approach of Slepian & Eisenstein (2015). Again, since we are working with a simulation box with periodic boundary conditions, it is possible to simplify the evaluation of the coefficients $\hat{\zeta}_\ell(r_{12}, r_{13})$ and derive an analytical expression for the monopole of the random triplet counts $N_{\mathrm{RRR},0}$.

The SHD estimator is known to be less efficient for isosceles or nearly isosceles triangle configurations (i.e. with $r_{12} \simeq r_{13}$). In these cases, a large value of ℓ_max is required to recover results consistent with those of the standard, direct-counting, estimator. Indeed, for isosceles triangles each coefficient of the expansion in Eq. (10) is the result of an integration over the bispectrum down to small, non-linear scales, beyond the range of validity of the perturbative model. On the other hand, using a fixed ℓ_max ensures internal consistency between measurements and theory. To mitigate this issue, we introduced the quantity (see e.g. Veropalumbo et al. 2022)

$$\eta := \frac{r_{13} - r_{12}}{\Delta r}, \tag{40}$$

with Δr being the separation bin size, to parametrise the proximity of a given configuration to the isosceles case. Fixing a lower limit (η_min) amounts to excluding isosceles, or nearly isosceles configurations.

In the bottom panels of Fig. 1 we present the 3PCF measurements for the four snapshots. The triangle index is defined by increasing value of r_{12}, r_{13}, and r_{23} under the condition $r_{12} \leq r_{13} \leq r_{23}$, as depicted in Fig. A.1. The measurements include all configurations with side lengths from $r_\mathrm{min} = 0\,h^{-1}$ Mpc to

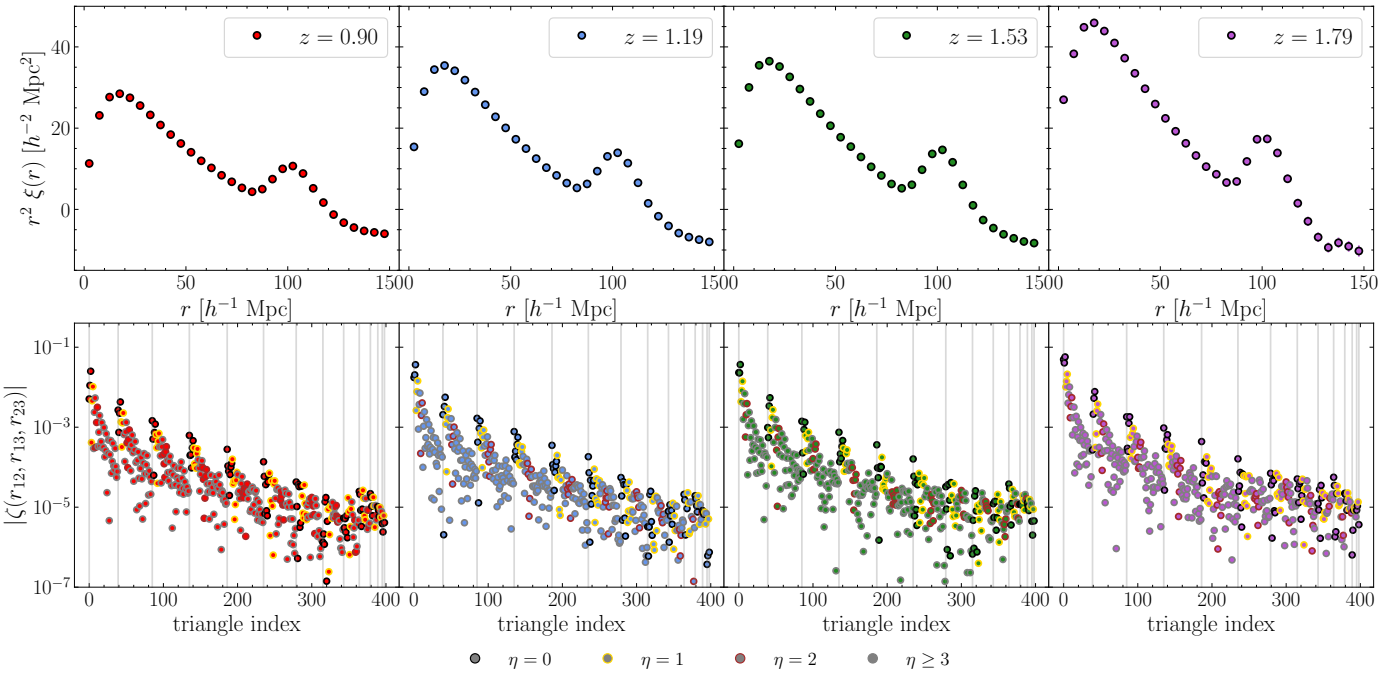

Fig. 1. *Top panels*: 2PCF measurements for four comoving snapshots from the Flagship I simulation of the Model 3 HOD. *Bottom panels*: Same but for the 3PCF measurements. The triangular configurations are ordered by increasing values of r_{12}, r_{13}, and r_{23} under the condition $r_{12} \leq r_{13} \leq r_{23}$, as depicted in Fig. A.1. The circles are colour-coded according to the η, while the vertical grey lines mark a group of triangles that share the same value of the smaller side (r_{12}).

$r_{\rm max} = 150\,h^{-1}$ Mpc in bins of width $\Delta r = 5\,h^{-1}$ Mpc. We expanded the 3PCF up to $\ell_{\rm max} = 10$, which strikes an ideal balance between computational efficiency and information content. A more detailed description of the numerical implementation and validation of the SHD estimator for the 3PCF will be given in Euclid Collaboration: Veropalumbo et al. (in prep.), while a similar presentation of the 2PCF estimator is given in Euclid Collaboration: de la Torre et al. (2025).

4.3. Covariance

We made use of a covariance matrix obtained from an analytical model for both two- and three-point functions. We worked in the Gaussian approximation, so all covariance depends simply on the galaxy power spectrum, and we further assumed a linear model for this spectrum.

For the 2PCF covariance we have (Grieb et al. 2016; Lippich et al. 2019)

$$C_\xi(r, r') = \frac{1}{\pi^2 V} \int_0^\infty {\rm d}k\, k^2\, P_{\rm tot}^2(k)\, \bar{j}_0(kr)\, \bar{j}_0(kr'), \tag{41}$$

where V is the box volume, $\bar{j}_0$ are the bin-averaged, zeroth-order Bessel functions (see Eq. A19 in Grieb et al. 2016), while

$$P_{\rm tot}(k) := b_1^2\, P_{\rm lin}(k) + \frac{1}{\bar{n}_g} \tag{42}$$

is the linear galaxy power spectrum including a Poisson shot-noise contribution, $\bar{n}_g$ being the galaxy number density. For each redshift snapshot, we computed the covariance matrix using the bias and density values listed in Table 2. As noted by Smith (2009), a more detailed treatment of discrete tracers introduces additional terms in the covariance – particularly relevant at low number density – even under Gaussian assumptions. These include contributions from combinatoric sampling effects, which are not included in our model; this is sufficient given the number density of the simulated dataset.

For the 3PCF covariance, we followed the expression proposed in Slepian & Eisenstein (2015), rigorously validated in Veropalumbo et al. (2022). This again takes advantage of the SHD writing the covariance between two measurements $\hat{\zeta}(r_{12}, r_{13}, r_{23})$ and $\hat{\zeta}(r'_{12}, r'_{13}, r'_{23})$ as

$$\begin{aligned} &C_\zeta(r_{12}, r_{13}, r_{23}; r'_{12}, r'_{13}, r'_{23}) = \\ &\quad = \sum_{\ell,\ell'}^{\ell_{max}} C_{\zeta,\ell\ell'}(r_{12}, r_{13}; r'_{12}, r'_{13})\, \mathcal{L}_\ell(\mu_{12,13})\, \mathcal{L}_{\ell'}(\mu_{12,13}), \end{aligned} \tag{43}$$

where $C_{\zeta,\ell\ell'}(r_{12}, r_{13}; r'_{12}, r'_{13})$ represents the covariance between the coefficients $\hat{\zeta}_\ell(r_{12}, r_{13})$ and $\hat{\zeta}_{\ell'}(r_{12}r_{12}, r_{13}r_{12})$. This, in turn, is given by

$$\begin{aligned} &C_{\zeta,\ell\ell'}(r_i, r_j; r'_i, r'_j) = \\ &= \frac{(2\ell+1)\,(2\ell'+1)\,(-1)^{\ell+\ell'}}{(2\pi)^6\, V} \int {\rm d}p_1\, {\rm d}p_2\, {\rm d}p_3\, \delta_{\rm D}(\mathbf{p}_{123}) \\ &\quad \times P_{\rm tot}(p_1)\, P_{\rm tot}(p_2)\, P_{\rm tot}(p_3)\, \bar{j}_\ell(p_1 r_i)\, \bar{j}_\ell(p_2 r_j)\, \mathcal{L}_\ell(\mu_{12}) \\ &\quad \times \left[\bar{j}_{\ell'}(p_1 r'_i)\, \bar{j}_{\ell'}(p_2 r'_j)\, \mathcal{L}_{\ell'}(\mu_{12}) + 5\ \text{perm.}\right]. \end{aligned} \tag{44}$$

We refer the reader to Slepian & Eisenstein (2015) for a detailed description of the practical evaluation of this expression.

In the Gaussian approximation, the cross-covariance between the two- and three-point functions vanishes, as the only contributions arise from the bispectrum of the density field and the connected 5-point function (see e.g. Sefusatti et al. 2006). While these terms are expected to introduce non-negligible correlations – potentially at the ~20% level for amplitude-related parameters – we neglected them in this work for consistency

with the Gaussian covariance framework. This choice is justified by the scope of our analysis, which focuses on validating the modelling pipeline rather than delivering optimal cosmological constraints.

5. Likelihood analysis and performance metrics

We define in the section the likelihood function we adopted to fit the parameters of our model to the simulation measurements. We also introduce the statistical tools we used to determine the range of validity of the model in terms of the GoF, the level of theoretical uncertainties introduced by the model, and the ability to constrain cosmological parameters.

5.1. Likelihood function

We adopted a Gaussian likelihood function for both the 2PCF and the 3PCF measurements. We thus have

$$-2\ln\mathcal{L}_\xi(\theta) = \chi^2_\xi(\theta), \tag{45}$$

where vector θ denotes the model parameters while the χ^2 for the 2PCF is given by

$$\chi^2_\xi(\theta) = \sum_{i,j=1}^{N_r} [\xi_i(\theta) - \hat{\xi}_i]\, C^{-1}_{\xi,ij}\, [\xi_j(\theta) - \hat{\xi}_j], \tag{46}$$

with $\xi(\theta)$ and $\hat{\xi}$ representing respectively the 2PCF theoretical prediction and its measurements and with the sum running over the separation bins r_i and r_j, N_r being the total number of bins, corresponding to the size of the data vector. Similarly, for the 3PCF we have

$$-2\ln\mathcal{L}_\zeta(\theta) = \chi^2_\zeta(\theta), \tag{47}$$

with

$$\chi^2_\zeta(\theta) = \sum_{i,j=1}^{N_t} [\zeta_i(\theta) - \hat{\zeta}_i]\, C^{-1}_{\zeta,ij}\, [\zeta_j(\theta) - \hat{\zeta}_j], \tag{48}$$

with the sum now extending over all triangular configuration up to their total number (N_t).

The likelihood of joint measurements of the 2PCF and 3PCF is simply given by

$$\mathcal{L}_{\xi+\zeta}(\theta) = \mathcal{L}_\xi(\theta)\,\mathcal{L}_\zeta(\theta), \tag{49}$$

and, correspondingly, the joint χ^2 will be

$$\chi^2_{\xi+\zeta}(\theta) = \chi^2_\xi(\theta) + \chi^2_\zeta(\theta) \tag{50}$$

since, as mentioned above, we neglected the cross-covariance between the two statistics.

We sampled the posterior using the `emcee` code[2] (Foreman-Mackey et al. 2013), implementing an affine-invariant ensemble sampler, which is particularly well suited to high-dimensional parameter spaces. We employed 50 walkers in each run and ensured that the chains are terminated only after exceeding 100 integrated autocorrelation times, thereby ensuring full convergence.

The model parameters, along with uniform priors assumed in all likelihood evaluations, are outlined in Table 3. The choice of large intervals is meant to ensure uninformative priors.

[2] https://emcee.readthedocs.io/

Table 3. Cosmological and nuisance parameters of the 2PCF and 3PCF models.

Parameter	Prior
Cosmology	
$10^{-9}A_s$	$\mathcal{U}[1,3]$
h	$\mathcal{U}[0.50,0.80]$
$\omega_{\rm cdm}$	$\mathcal{U}[0.09,0.15]$
Nuisance parameters (bias and counterterm)	
b_1	$\mathcal{U}[1,5]$
b_2	$\mathcal{U}[-20,20]$
$b_{\mathcal{G}_2}$	$\mathcal{U}[-20,20]$ or fixed to Eq. (16)
b_{Γ_3}	$\mathcal{U}[-20,20]$ or fixed to Eq. (17)
c_0 $[h^{-2}\,\mathrm{Mpc}^2]$	$\mathcal{U}[-100,100]$

Notes. The table lists the cosmological and nuisance parameters used in the analysis described in Sect. 3. The last column provides the uniform priors adopted, or the bias relations used in some runs to reduce the parameter space.

5.2. Performance metrics

Our main goal is the assessment of the range of validity of the model, determining the minimum scale, $r_{\rm min}$, down to which the model can still accurately describe the measurements without introducing significant systematic uncertainties to the recovered cosmological parameters. As in the companion paper (Euclid Collaboration: Pezzotta et al. 2024), this task is carried out using three performance metrics: a GoF, a figure of bias (FoB), and figure of merit (FoM) as defined below.

5.2.1. Goodness of fit

For an assessment on the GoF, we simply used the standard χ^2 test. The χ^2 definitions for the 2PCF, 3PCF, and joint at a given point θ in the parameter space are given in Eqs. (46), (48), and (50). The posterior-averaged value, $\langle\chi^2\rangle_{\rm post}$, is then compared to the thresholds from the χ^2 distribution at the 68% and 95% confidence levels, determined in terms of the appropriate number of degrees of freedom, computed as the difference between the size of the data vector and the number of model parameters.

5.2.2. Figure of bias

We quantified the uncertainties in recovering a subset of fiducial, cosmological parameters ($\theta_{\rm fid}$) due to model systematic uncertainties in terms of an FoB defined as

$$\mathrm{FoB}(\theta) = \left[\left(\langle\theta\rangle_{\rm post} - \theta_{\rm fid}\right)^{\rm T} S^{-1}(\theta)\left(\langle\theta\rangle_{\rm post} - \theta_{\rm fid}\right)\right]^{1/2}, \tag{51}$$

where $\langle\theta\rangle_{\rm post}$ represents the parameter averaged over the posterior distribution, while $S(\theta)$ is the parameters' covariance matrix, evaluated from the same posterior distribution.

When θ consists of a single parameter, the FoB measures the deviation of the posterior mean from the fiducial value in units of the parameter's standard deviation, with FoB values of one and two corresponding to the 68% and 95% confidence levels, respectively. However, when dealing with multiple parameters, these thresholds must be recalculated by integrating a multivariate normal distribution over the appropriate number of dimensions. For instance, in the case of three parameters relevant for the results of Sect. 7, the 68% and 95% confidence levels correspond to FoB values of 1.87 and 2.80, respectively.

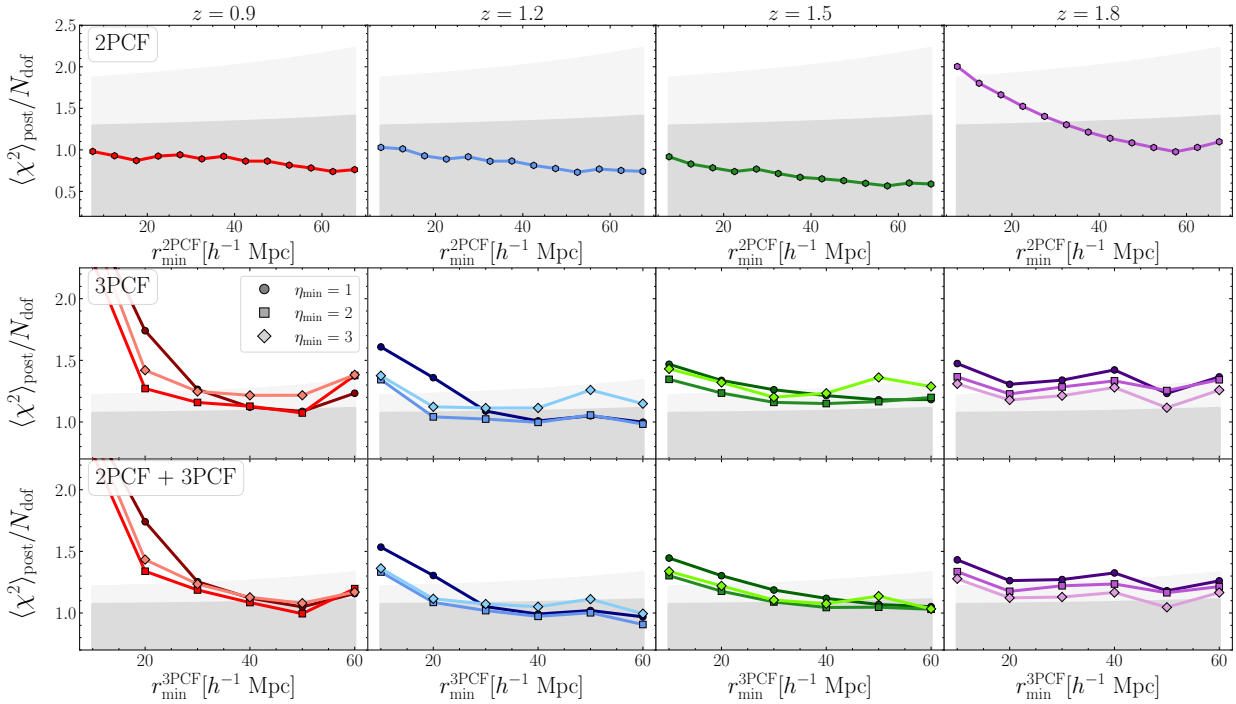

Fig. 2. GoF test for the bias 2PCF and 3PCF models with fixed cosmological parameters as a function of the minimal scale, $r_{\rm min}^{\rm 2PCF}$ and $r_{\rm min}^{\rm 3PCF}$, respectively, assumed for the analysis. The posterior-averaged χ^2 is compared to the 68% and 95% confidence intervals for the χ^2 distribution, denoted by the grey shaded areas, given the corresponding $N_{\rm d.o.f.}$ (fixing the case $\eta_{\rm min} = 1$ for the 3PCF confidence levels; see the main text for more details). For the 3PCF, we considered three different values for the $\eta_{\rm min}$ parameter, Eq. (40), progressively excluding near-isosceles configurations. In the joint analysis, the minimal scale for the 2PCF was kept fixed at $r_{\rm min}^{\rm 2PCF} = 25\,h^{-1}$ Mpc, with the results shown as a function of $r_{\rm min}^{\rm 3PCF}$ alone. The four columns span the four simulation snapshots at redshifts (z) of 0.9, 1.2, 1.5, and 1.8.

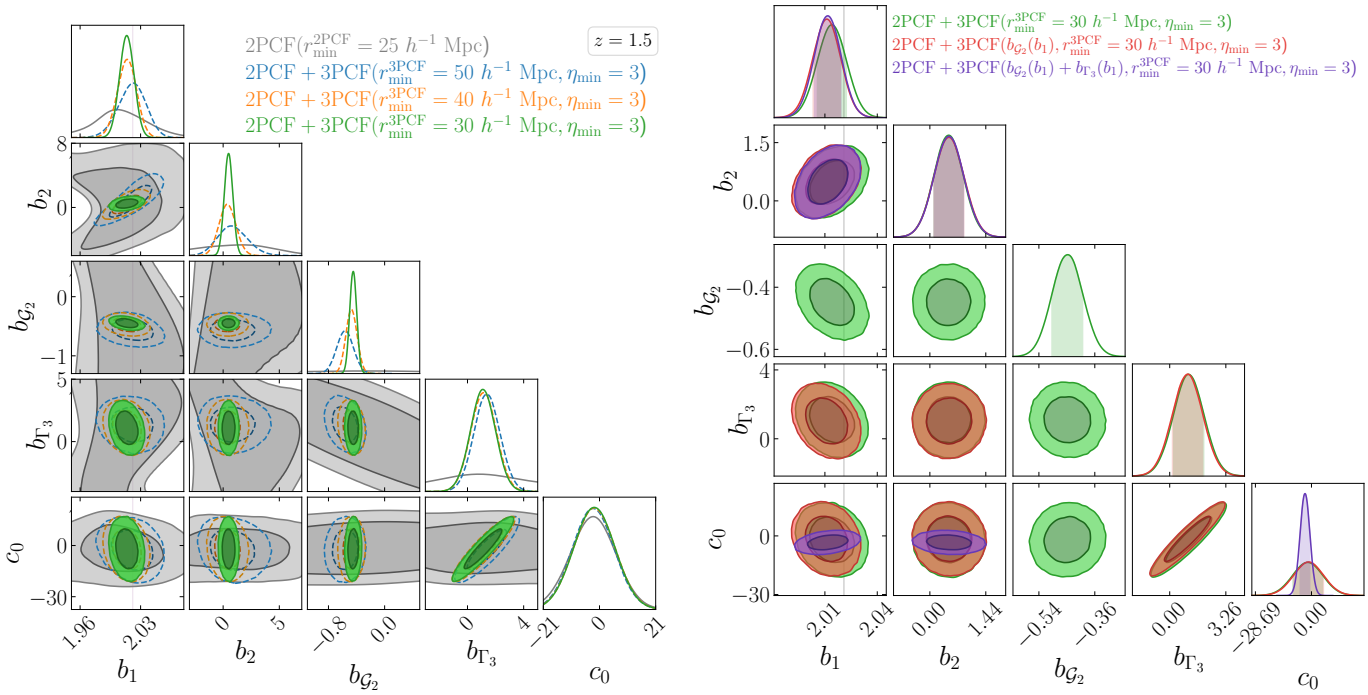

Fig. 3. *Left panel*: Marginalised 2D constraints at confidence intervals of 68.3% and 99.5%, on the nuisance parameters (bias and counter-term) from the 2PCF analysis (grey shaded areas) against the joint 2PCF and 3PCF analysis for several values of $r_{\rm min}^{\rm 3PCF}$ at $z = 1.5$ (dashed blue lines, dashed orange lines, and green shaded areas). All cases assume $\eta = 3$; see Eq. (40). The vertical grey band is an estimate of the linear bias b_1 obtained from a comparison of the galaxy power spectrum with measurements of the matter power spectrum in Euclid Collaboration: Pezzotta et al. (2024). *Right panel*: Marginalised 2D constraints at confidence intervals of 68.3% and 99.5%, on the nuisance parameters (bias and counter-term) from the joint 2PCF-3PCF analysis at $z = 1.5$ for $r_{\rm min}^{\rm 3PCF} = 30\,h^{-1}$ Mpc (red contours) compared to the same set-up but with the assumption of the $b_{\mathcal{G}_2}(b_1)$ bias relation alone (red contours) and the combination of the relations $b_{\mathcal{G}_2}(b_1)$ and $b_{\Gamma_3}(b_1)$ (violet contours).

5.2.3. Figure of merit

Finally, we defined an FoM (Albrecht et al. 2006; Wang 2008) to quantify the constraining power of our model over a specific range of scales and under given bias assumptions:

$$\mathrm{FoM}(\theta) = \frac{1}{\sqrt{\det[S(\theta)]}}, \tag{52}$$

where $\det[S(\theta)]$ is the determinant of the covariance matrix of the parameters of interest. This represents the hyper-volume enclosed by the hyper-surface defined by the covariance matrix $S(\theta)$. Therefore, a larger FoM indicates tighter constraints on the model parameters.

6. Galaxy bias

In this section we assess the range of validity of our bias model for both the 2PCF and 3PCF. Our focus will be then on the GoF test, keeping fixed the cosmological parameters at their fiducial values. We considered both the case where all bias parameters are free and the case where the bias relations mentioned above is assumed to reduce the parameter space. We also needed to make sure that no significant running of the bias parameters was present, i.e. there was no significant variation in the recovered parameters, as a function of the minimal scale defining the data vectors.

6.1. Maximal model

We started with the maximal model (see e.g. Oddo et al. 2021), with all bias parameters free, with the priors given in Table 3. In Fig. 2 we show the χ^2 averaged over the posterior distribution for the four redshift snapshots and for the 2PCF, 3PCF, and joint 2PCF+3PCF data vector.

We notice in the first place that while the one-loop 2PCF model provides a good fit for all scales considered, the tree-level 3PCF prediction fails for separations below $20\,h^{-1}$ Mpc at $z = 0.9$, with a better performance at higher redshift. Under the choice of $\eta_{\rm min} = 1$, Eq. (40), including configurations closer to the isosceles case, the validity of the model is further restricted to $r_{\rm min} > 20\,h^{-1}$ Mpc at $z = 0.9$ and $r_{\rm min} > 10\,h^{-1}$ Mpc for $z = 1.2$ and above.

In Fig. 3 we show the marginalised 2D constraints on the nuisance parameters (bias and counter-term) from the 2PCF analysis against the joint 2PCF plus 3PCF analysis for several values of $r_{\rm min}^{\rm 3PCF}$. This shows in the first place the peculiar and significant constraining power of higher-order statistics on linear and non-linear bias. This is particularly evident in the reduction of the posterior uncertainty on the non-linear parameter b_2 and non-local parameters $b_{\mathcal{G}_2}$ and b_{Γ_3}. It further shows that down to $r_{\rm min}^{\rm 3PCF} = 30\,h^{-1}$ Mpc no running of the bias parameter is evident, with all analyses at different $r_{\rm min}$ consistently reducing the posterior uncertainty.

The plots include, as a vertical grey band, an estimate of the value of the linear bias b_1 obtained from a comparison of the galaxy power spectrum with measurements of the matter power spectrum in Euclid Collaboration: Pezzotta et al. (2024). We find that the inclusion of the 3PCF consistently yields posterior distributions for b_1 that are visually closer to the reference value across all the minimum scale cuts explored. While the 2PCF-only results remain statistically consistent, they exhibit broader posteriors, reflecting a stronger degeneracy with other model parameters. We revisit this aspect in the context of cosmological parameter constraints in the following section.

6.2. Bias relations

The right panel of Fig. 3 shows the same results for the joint analysis with $r_{\rm min} = 30\,h^{-1}$ Mpc and $\eta_{\rm min} = 3$ (green contours), here compared to the same set-up but with the additional assumptions of two bias relations. We considered, in particular, the $b_{\mathcal{G}_2}(b_1)$ relation alone, Eq. (16), (red contours) and its combination with the relation for b_{Γ_3} of Eq. (17). We display only the results for the $z = 1.5$ snapshots, noticing that for the measurements at other redshifts we obtain qualitatively similar results.

We notice that in both cases, the bias relations provide a reduction of the parameter space by one and two parameters, respectively, without affecting the b_1, b_2 constraints. On this specific contour in fact we do not observe any induced systematic shift as we do not notice any appreciable reduction in the uncertainty. This is noticeable instead on the c_0 parameter, describing the combined effect of the EFT counter-term and higher derivative bias. These results provide some evidence that the bias relations can be used to speed up the likelihood evaluation without compromising the main results. We return to this point when discussing cosmological parameters constraints.

We close the section by noticing that the adoption of one or two bias relations does not lead to any worsening of the GoF, in terms of the χ^2 test. We avoid a dedicated figure since the difference with the maximal model case would be barely visible.

7. Cosmological parameters from the joint, full-shape analysis

In this section we present the results for the full-shape, joint analysis of 2PCF and 3PCF aiming at constraining three cosmological parameters: the amplitude of scalar fluctuations ($A_{\rm s}$), the CDM density ($\omega_{\rm cdm}$), and the Hubble constant (h). This minimal set captures the main physical effects to which large-scale structure observables are directly sensitive: $A_{\rm s}$ determines the amplitude of fluctuations and is probed by the power spectrum and bispectrum; $\omega_{\rm cdm}$ governs the growth history and the shape of the clustering signal; and h fixes the physical scales through the matter–radiation equality scale and the sound horizon, affecting the shape of correlation functions in real space. Limiting our analysis to these parameters highlights the constraining power of the full-shape information.

To the best of our knowledge, this is the first attempt at estimating the improvement due to adding the 3PCF to the full-shape analysis of the 2PCF, although still limited to real space. Until now, 3PCF analyses have been restricted to template fitting, i.e. using fixed-shape models to extract cosmological information from the BAO scale position or from the anisotropy induced by redshift-space distortions, rather than performing full-shape parameter inference, due to the considerable computational demands of a full cosmology-dependent 3PCF model.

A key ingredient, to achieve this goal, is the emulator described in Appendix B. Constructed using a `PyTorch`[3] framework, the emulator has undergone extensive testing and has been fully integrated into the same sampler. The emulator extends to the 2PCF prediction, further enhancing the overall efficiency of our analysis.

[3] https://pytorch.org/docs/stable/index.html

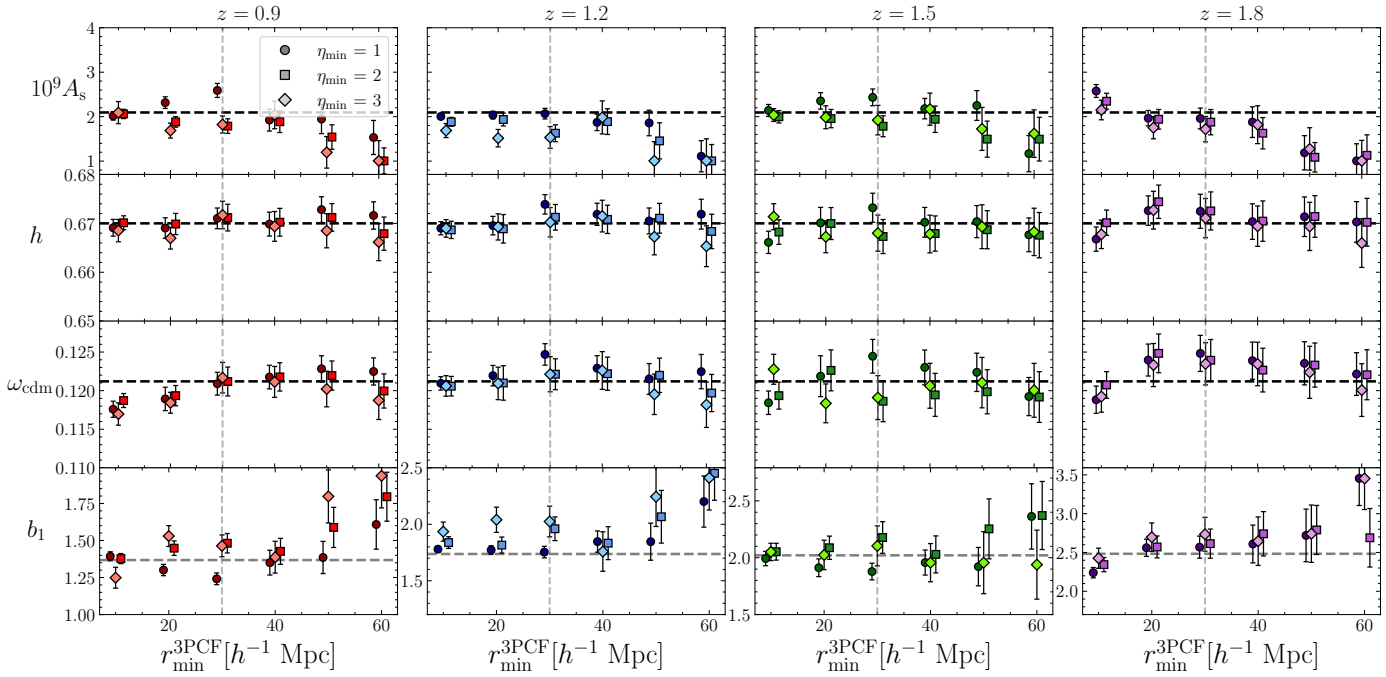

Fig. 4. Marginalised constraints on the cosmological parameters and linear bias from a joint 2PCF and 3PCF analysis. The posterior mean along with its uncertainties is displayed as a function of the minimal scale ($r_{\rm min}^{\rm 3PCF}$) for different choices of $\eta_{\rm min}$ and fixing $r_{\rm min}^{\rm 2PCF} = 25\,h^{-1}$ Mpc and $r_{\rm max} = 140\,h^{-1}$ Mpc for both statistics. The dashed black line refers to the fiducial values assumed in the simulation, while the dashed grey line refers to the fiducial b_1 adopted in Euclid Collaboration: Pezzotta et al. (2024), also shown in Fig. 3.

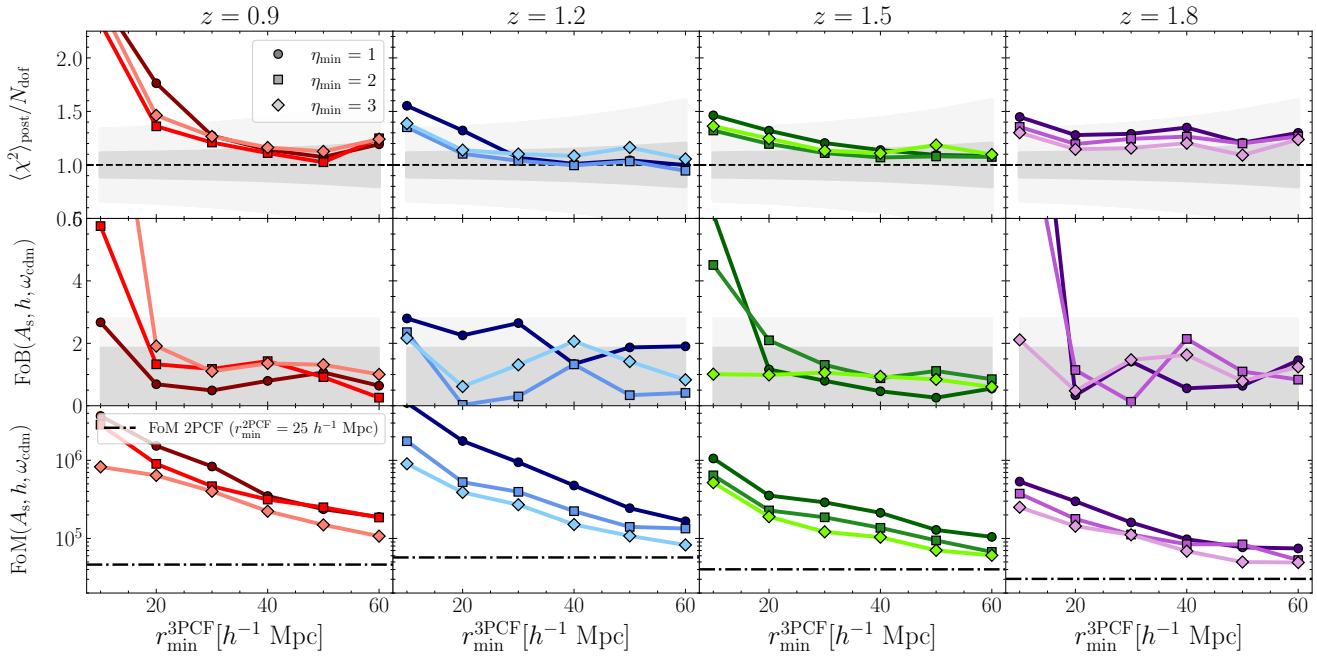

Fig. 5. Performance metrics for the full-shape, joint analysis of the 2PCF and the 3PCF. All quantities are shown as a function of the minimal scale ($r_{\rm min}^{\rm 3PCF}$), with $r_{\rm min}^{\rm 2PCF}$ fixed at 25 h^{-1} Mpc, and for the three different values of $\eta_{\rm min}$ in different colour shades. From top to bottom we show the posterior-averaged $\langle \chi^2 \rangle_{\rm post}$ for the GoF, the FoB, and the FoM, these last two both defined in terms of the three cosmological parameters $A_{\rm s}$, $\omega_{\rm cdm}$, and h. The grey bands denote the 68% and 99.7% confidence levels for the χ^2 distribution and the FoB.

Figure 4 shows marginalised constraints on cosmological parameters $A_{\rm s}$, $\omega_{\rm cdm}$, h, and on the linear bias b_1 derived from the joint 2PCF and 3PCF analysis as a function of the minimal scale $r_{\rm min}$ that characterises the 3PCF data vector, with the minimal separation in the 2PCF measurements fixed at $r_{\rm min}^{\rm 2PCF} = 25\,h^{-1}$ Mpc. The four columns span the different redshifts. As in Fig. 2, varying shades of these colours correspond to different choices for the parameter $\eta_{\rm min}$. The dashed black lines denote the fiducial values assumed for the simulations, together with the grey line that shows the same fiducial values for b_1 considered

in Fig. 3. Overall, the results show good agreement between the emulated predictions and the expected values. For large values of $r_{\rm min}$, the estimates for $A_{\rm s}$ and b_1 tend to deviate further from the expected values, largely due to projection effects caused by a large degeneracy between these parameters. On the other hand, moving to the small-scale regime, a possible failure of the model to recover the fiducial values is only evident for $\omega_{\rm cdm}$ at the lowest redshift of $z = 0.9$. Below $r_{\rm min} = 40\,h^{-1}$ Mpc, the estimates for $A_{\rm s}$ and $b_1(z)$ exhibit a slight dependence on the choice of $\eta_{\rm min}$, with the case of $\eta_{\rm min} = 1$ leading to more biased values for these parameters, particularly at low redshift.

In Fig. 5 we present the performance metrics corresponding to the results of Fig. 4, all as a function of the minimal scales $r_{\rm min}^{\rm 3PCF}$, with $r_{\rm min}^{\rm 2PCF}$ fixed at 25 h^{-1} Mpc, and for the same three different values of $\eta_{\rm min}$. The top panels show the posterior-averaged $\langle\chi^2\rangle_{\rm post}$. The grey bands denote the 68% and 99.7% confidence levels for the χ^2 distribution. We find a good fit for $r_{\rm min}^{\rm 3PCF} \gtrsim 20\,h^{-1}$ Mpc except for the lowest redshift where $r_{\rm min}^{\rm 3PCF} \gtrsim 30\,h^{-1}$ Mpc ensures a safer result. This is naturally consistent with the results at fixed cosmology. The middle panels show the FoB, defined in terms of the parameters $A_{\rm s}$, $\omega_{\rm cdm}$, and h. The uncertainties are shown again in two shades of grey, corresponding to 68% and 95% confidence levels. The model provides overall unbiased results except for the first separation bin at $r_{\rm min} = 10\,h^{-1}$ Mpc, for all redshifts and for all values of $\eta_{\rm min}$. Finally, the bottom panels of Fig. 5 show the FoM, defined again in terms of the three cosmological parameters. The FoM increases significantly across the whole separation range (notice the log-scale on the y-axis) and presents also larger values in the lowest redshift snapshots. In addition, the choice of a low value for $\eta_{\rm min}$ can also make a large difference, since this increase the size of the data vector and relative S/N.

The left plot of Fig. 6 shows the constraints on the cosmological parameters at $z = 0.9$ plus the linear bias obtained from the combined statistics for different choices of $r_{\rm min}^{\rm 3PCF}$ and $\eta_{\rm min}$, compared to the 2PCF-only constraints where we include an additional, informative Gaussian prior on b_1 for illustrative purposes defined by a 10% error on the best-fit value obtained from the joint analysis. This is required by the strong degeneracy between $A_{\rm s}$ and b_1 in the 2PCF likelihood. This degeneracy is still present in the joint analysis, although significantly reduced without imposing any prior on b_1. We obtain a discrepancy with the fiducial value of $A_{\rm s}$ at confidence interval of 68.3% for the configuration with $r_{\rm min}^{\rm 3PCF} = 30\,h^{-1}$ Mpc and $\eta_{\rm min} = 2$, while the discrepancy is smaller for the other parameters, despite the additional degeneracy between h and $\omega_{\rm cdm}$. Interestingly, no tension is visible on the h and $\omega_{\rm cdm}$ constraints.

The same results are found with no relevant difference for all snapshots, as described in Fig. C.1. We remind the reader that the posterior distributions are not statistically independent since each realisation is a different snapshot of the same evolving dark matter perturbations, sharing the same initial seeds. We observe that at lower redshifts the constraints are tighter due to the larger density of the galaxy distribution and that, in general, both h and $\omega_{\rm cdm}$ exhibit accurate estimates of the fiducial values. The largest discrepancy, at the limit of the confidence interval of 99.5% contour, is obtained for $A_{\rm s}$ at $z = 1.2$. We notice that now also the linear bias parameter is correctly recovered at all redshifts.

In the right plot of Fig. 6, we compare the maximal model with all free parameters, assuming $r_{\rm min}^{\rm 3PCF} = 30\,h^{-1}$ Mpc and $\eta_{\rm min} = 3$, to the results obtained assuming the bias relation of Eq. (16) for $b_{\mathcal{G}_2}$, and its combination with the relation for b_{Γ_3} of Eq. (17), showing the same set of parameters as in the right plot. Overall, we notice how the adoption of the bias relations enhances the precision of the cosmological parameter constraints. Notably, the 2D posterior distribution of $A_{\rm s}$ and b_1, affected by a strong degeneracy, benefits the most from this additional information, although, again, we notice a slightly biased estimate for $A_{\rm s}$. As presented in Fig. C.2, which shows the full set of parameters, the b_{Γ_3} relation greatly reduces the uncertainty on the higher derivatives and/or counter-term parameter c_0, as in the bias-only case.

8. Conclusions

In this work we provide a validation of PT models for the 2PCF and 3PCF in real space across a redshift range and against a synthetic galaxy catalogue representative of the *Euclid* spectroscopic galaxy survey (see e.g. Euclid Collaboration: Mellier et al. 2025).

We took advantage of galaxy clustering measurements obtained from four redshift snapshots of the Flagship I simulation populated with the HOD following the Model 3 prescription of Pozzetti et al. (2016). In particular, we determined HOD parameters by selecting galaxies with a Hα flux limit of $f_{\rm H\alpha} = 2 \times 10^{-16}$ erg cm^{-2} s^{-1}. The 3PCF measurements in particular, presented in Sect. 4, are based on the SHD introduced by Slepian & Eisenstein (2015); see also Euclid Collaboration: Veropalumbo et al. (in prep). This estimator allowed us to measure all 3PCF configurations while keeping a manageable computational cost.

The galaxy 2PCF is modelled at the NLO within the framework of EFTofLSS, involving up to five nuisance parameters: b_1, b_2, $b_{\mathcal{G}_2}$, b_{Γ_3}, and the parameter c_0, which describes an EFT counter-term and higher-derivative bias. The 3PCF, on the other hand, was modelled at the LO in PT, with the tree-level expression depending only on the bias parameters b_1, b_2, and $b_{\mathcal{G}_2}$.

We first assessed the GoF provided by the model via a χ^2 test and explored its range of validity as a function of the minimal scale included in the data vector and of the additional parameter $\eta_{\rm min}$ Eq. (40), progressively excluding nearly isosceles triangles from the analysis (Sect. 6). The predictions for these configurations are, in fact, affected by systematic uncertainties when the Legendre expansion of Eq. (10) is limited to a relatively small number of multipoles, as in any practical application. We find that the tree-level model for the 3PCF fails below separations of $20\,h^{-1}$ Mpc when $\eta_{\rm min} \geq 2$, while a larger minimum scale should be considered for when $\eta_{\rm min} = 1$. Commonly adopted relations between bias parameters, such as those for $b_{\mathcal{G}_2}(b_1)$ and $b_{\Gamma_3}(b_1)$, can help reduce the parameter space without affecting the determination of the other bias parameters, except for the c_0 parameter.

The main results of the paper, presented in Sect. 7, are from a joint, full-shape analysis of the 2PCF and 3PCF, carried out with the aim of constraining three cosmological parameters: A_s, $\omega_{\rm cdm}$, and h. Cosmological analyses involving the 3PCF have so far been based on template fitting (see e.g. Slepian et al. 2017; Slepian & Eisenstein 2018; Veropalumbo et al. 2021; Sugiyama et al. 2021; Farina et al. 2026), as a direct evaluation of the 3PCF model is computationally too expensive. To overcome this hurdle, we developed an emulator able to provide fast and accurate full predictions for both 2PCF and 3PCF, thereby enabling a complete joint analysis of the two statistics.

In this case, in addition to the χ^2 test, we adopted an FoB and an FoM to quantify the model's systematic uncertainties along with its ability to constrain cosmological parameters. Focusing

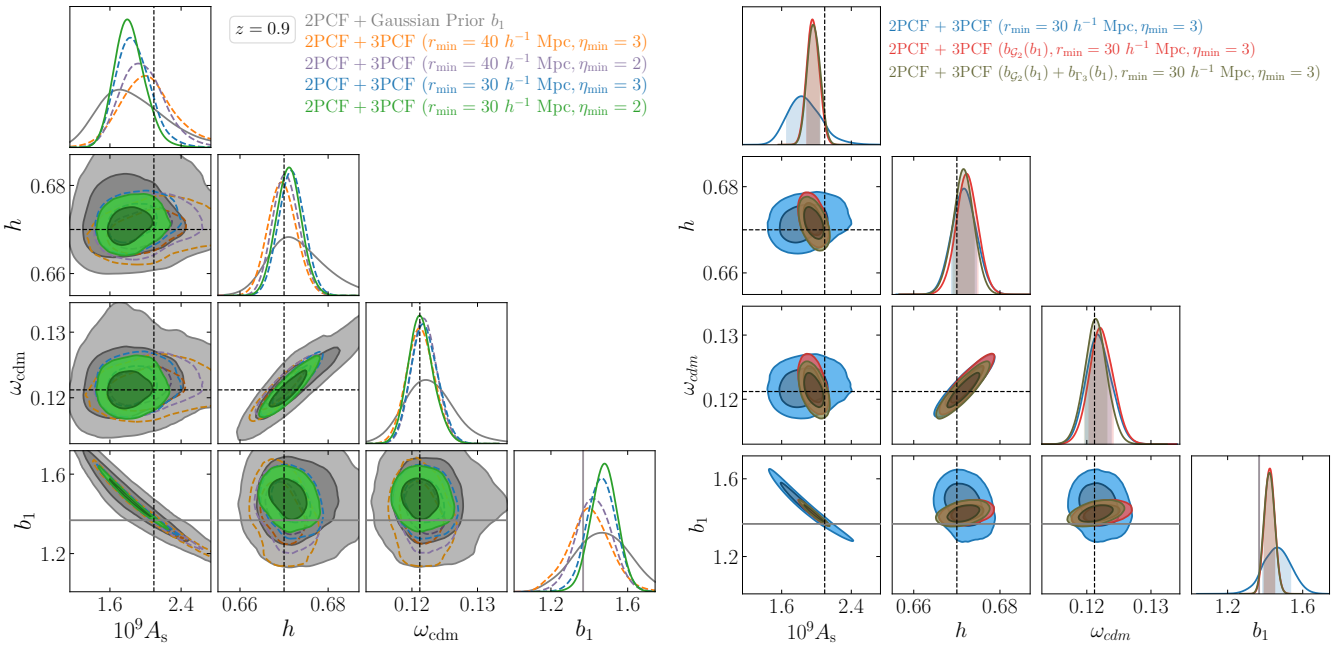

Fig. 6. *Left panel*: Marginalised 2D and 1D posterior distributions at $z = 0.9$ from the joint 2PCF and 3PCF analysis of the cosmological parameters h, $\omega_{\rm cdm}$, and $A_{\rm s}$ and the linear bias parameter b_1 for various 3PCF scale cuts ($r_{\rm min}^{\rm 3PCF}$) and the $\eta_{\rm min}$ parameter defined in Eq. (40), fixing $r_{\rm min}^{\rm 2PCF} = 25\,h^{-1}$ Mpc. Grey contours correspond to the 2PCF-only analysis assuming a Gaussian prior on b_1 given by the 10% uncertainties around the best-fit value obtained from the joint analysis. Each panel shows the results for a different snapshot. Vertical and horizontal lines denote the fiducial values of the cosmological parameters. *Right panel*: Marginalised 1D and 2D posterior distributions of the same subset of model parameters for the combined analysis of 2PCF and 3PCF at $z = 0.9$ fixing $r_{\rm min}^{\rm 2PCF} = 25\,h^{-1}$ Mpc. The reference case of the maximal model with $r_{\rm min}^{\rm 3PCF} = 30\,h^{-1}$ Mpc and $\eta_{\rm min} = 3$ is compared to the results obtained adopting the bias relations of Eq. (16), in red, and its combination with Eq. (17), in brown.

only on the results for the joint analysis, since only this configuration allows us to properly constrain all three parameters without informative priors, we find that a conservative choice for the scale cuts is given by $r_{\rm min}^{\rm 3PCF} = 40\,h^{-1}$ Mpc and $\eta_{\rm min} = 3$. A more aggressive configuration with $r_{\rm min}^{\rm 3PCF} = 30\,h^{-1}$ Mpc and $\eta_{\rm min} = 2$ is still acceptable, although a tension at the confidence interval of 68.3% with the fiducial value A_s begins to show. This finding aligns with conclusions drawn from previous methodological studies on the galaxy bias model (see e.g. Veropalumbo et al. 2022, for further details). On the other hand, selecting $\eta_{\rm min} = 1$ led to more unstable results, particularly at lower redshifts.

Adopting bias relations provides only a limited advantage in a bias-only analysis. However, when cosmological parameters are included, it can lead to tighter constraints, most notably on A_s, particularly in the case of Eq. (16).

In conclusion, we confirm that, as expected, the combination of 2PCF and 3PCF in real space provides greater constraining power with respect to the 2PCF alone, effectively breaking the degeneracy between A_s and $b_1(z)$. We also expect the improvement to be less pronounced in redshift space, where the 2PCF multipoles typically show reduced degeneracies among cosmological and bias parameters. This work represents a first step towards a full-shape joint analysis in redshift space that, out of necessity, will require tools such as the emulator developed here. In this perspective, this study paves the way for the application of emulated predictions in comparisons to real data, setting the stage for a complete analysis of galaxy clustering data in configuration space that will be on the same footing as power spectrum and bispectrum joint analyses.

This work is part of a series of preparation papers aimed at validating theoretical models for the analysis of galaxy clustering statistics from the *Euclid* spectroscopic sample. A first assessment of the real-space model for the galaxy power spectrum has been presented in Euclid Collaboration: Pezzotta et al. (2024). The cases of the redshift space power spectrum and 2PCF will be presented respectively in Euclid Collaboration: Camacho et al. (in prep.) and Euclid Collaboration: Kärcher et al. (in prep.). In addition, the redshift-space, joint power spectrum and bispectrum, and 2PCF-3PCF cases will appear in Euclid Collaboration: Pardede et al. (in prep.) and Euclid Collaboration: Pugno et al. (in prep.). Finally, another study will explore the BAO signal in the redshift-space 3PCF.

Acknowledgements. We thank Krister Nagainis, Adi Nusser and Andrea Enia for useful discussions. MG and MM acknowledge support from the research grant 'Optimizing the extraction of cosmological information from Large Scale Structure analysis in view of the next large spectroscopic surveys' from MIUR, PRIN 2022 (grant 2022NY2ZRS 001). MM acknowledges the financial contribution from the grant ASI n. 2024-10-HH.0 "Attività scientifiche per la missione Euclid – fase E. The Euclid Consortium acknowledges the European Space Agency and a number of agencies and institutes that have supported the development of *Euclid*, in particular the Agenzia Spaziale Italiana, the Austrian Forschungsförderungsgesellschaft funded through BMK, the Belgian Science Policy, the Canadian Euclid Consortium, the Deutsches Zentrum für Luft- und Raumfahrt, the DTU Space and the Niels Bohr Institute in Denmark, the French Centre National d'Etudes Spatiales, the Fundação para a Ciência e a Tecnologia, the Hungarian Academy of Sciences, the Ministerio de Ciencia, Innovación y Universidades, the National Aeronautics and Space Administration, the National Astronomical Observatory of Japan, the Netherlandse Onderzoekschool Voor Astronomie, the Norwegian Space Agency, the Research Council of Finland, the Romanian Space Agency, the State Secretariat for Education, Research, and Innovation (SERI) at the Swiss Space Office (SSO), and the United Kingdom

Space Agency. A complete and detailed list is available on the *Euclid* web site (www.euclid-ec.org).

References

Adame, A. G., Aguilar, J., Ahlen, S., et al. 2025, JCAP, 02, 021
Albrecht, A., Bernstein, G., Cahn, R., et al. 2006, arXiv e-prints [arXiv:astro-ph/0609591]
Assassi, V., Baumann, D., Green, D., & Zaldarriaga, M. 2014, JCAP, 08, 056
Baldauf, T., Seljak, U., Desjacques, V., & McDonald, P. 2012, Phys. Rev. D, 86, 083540
Baldauf, T., Mirbabayi, M., Simonović, M., & Zaldarriaga, M. 2015, Phys. Rev. D, 92, 043514
Bardeen, J. M., Bond, J. R., Kaiser, N., & Szalay, A. S. 1986, ApJ, 304, 15
Baumann, D., Nicolis, A., Senatore, L., & Zaldarriaga, M. 2012, JCAP, 07, 051
Bernardeau, F., Colombi, S., Gaztañaga, E., & Scoccimarro, R. 2002, Phys. Rep., 367, 1
Beutler, F., Seo, H.-J., Saito, S., et al. 2017, MNRAS, 466, 2242
Blas, D., Garny, M., Ivanov, M. M., & Sibiryakov, S. 2016a, JCAP, 07, 052
Blas, D., Garny, M., Ivanov, M. M., & Sibiryakov, S. 2016b, JCAP, 07, 028
Cabass, G., Ivanov, M. M., Philcox, O. H. E., Simonović, M., & Zaldarriaga, M. 2022, Phys. Rev. Lett., 129, 021301
Carrasco, J. J. M., Hertzberg, M. P., & Senatore, L. 2012, J. High Energy Phys., 9, 82
Catelan, P., Lucchin, F., Matarrese, S., & Porciani, C. 1998, MNRAS, 297, 692
Chan, K. C., Scoccimarro, R., & Sheth, R. K. 2012, Phys. Rev. D, 85, 083509
Coles, P., Moscardini, L., Lucchin, F., Matarrese, S., & Messina, A. 1993, MNRAS, 264, 749
Crocce, M., & Scoccimarro, R. 2008, Phys. Rev. D, 77, 023533
D'Amico, G., Gleyzes, J., Kokron, N., et al. 2020, JCAP, 05, 005
D'Amico, G., Lewandowski, M., Senatore, L., & Zhang, P. 2025, Phys. Rev. D, 111, 063514
Dawson, K. S., Schlegel, D. J., Ahn, C. P., et al. 2013, AJ, 145, 10
DESI Collaboration (Aghamousa, A., et al.) 2016, arXiv e-prints [arXiv:1611.00036]
Desjacques, V. 2008, Phys. Rev. D, 78, 103503
Desjacques, V., Crocce, M., Scoccimarro, R., & Sheth, R. K. 2010, Phys. Rev. D, 82, 103529
Desjacques, V., Jeong, D., & Schmidt, F. 2018, Phys. Rep., 733, 1
Dore, O., Hirata, C., Wang, Y., et al. 2019, BAAS, 51, 341
Eggemeier, A., Scoccimarro, R., & Smith, R. E. 2019, Phys. Rev. D, 99, 123514
Eggemeier, A., Scoccimarro, R., Crocce, M., Pezzotta, A., & Sánchez, A. G. 2020, Phys. Rev. D, 102, 103530
Eisenstein, D. J., Zehavi, I., Hogg, D. W., et al. 2005, ApJ, 633, 560
Eisenstein, D. J., Seo, H.-J., & White, M. 2007, ApJ, 664, 660
Euclid Collaboration (Blanchard, A., et al.) 2020, A&A, 642, A191
Euclid Collaboration (Scaramella, R., et al.) 2022, A&A, 662, A112
Euclid Collaboration (Pezzotta, A., et al.) 2024, A&A, 687, A216
Euclid Collaboration (de la Torre, S., et al.) 2025, A&A, 700, A78
Euclid Collaboration (Mellier, Y., et al.) 2025, A&A, 697, A1
Euclid Collaboration (Risso, I., et al.) 2026, A&A, 707, A233
Fang, X., Eifler, T., & Krause, E. 2020, MNRAS, 497, 2699
Farina, A., Veropalumbo, A., Branchini, E., & Guidi, M. 2026, J. Cosmol. Astropart. Phys., 2026, 028
Foreman-Mackey, D., Hogg, D. W., Lang, D., & Goodman, J. 2013, PASP, 125, 306
Frieman, J. A., & Gaztanaga, E. 1994, ApJ, 425, 392
Fry, J. N. 1984, ApJ, 279, 499
Fry, J. N. 1994, Phys. Rev. Lett., 73, 215
Fry, J. N., & Gaztañaga, E. 1993, ApJ, 413, 447
Fujita, T., Mauerhofer, V., Senatore, L., Vlah, Z., & Angulo, R. 2020, JCAP, 01, 009
Gaztañaga, E., Norberg, P., Baugh, C. M., & Croton, D. J. 2005, MNRAS, 364, 620
Gaztañaga, E., Cabré, A., Castander, F., Crocce, M., & Fosalba, P. 2009, MNRAS, 399, 801
Gil-Marín, H., Percival, W. J., Verde, L., et al. 2017, MNRAS, 465, 1757
Grieb, J. N., Sánchez, A. G., Salazar-Albornoz, S., & Dalla Vecchia, C. 2016, MNRAS, 457, 1577
Grieb, J. N., Sánchez, A. G., Salazar-Albornoz, S., et al. 2017, MNRAS, 467, 2085
Guidi, M., Veropalumbo, A., Branchini, E., Eggemeier, A., & Carbone, C. 2023, JCAP, 08, 066
Guzzo, L., Pierleoni, M., Meneux, B., et al. 2008, Nature, 451, 541
Hamilton, A. J. S. 2000, MNRAS, 312, 257
Hivon, E., Bouchet, F. R., Colombi, S., & Juszkiewicz, R. 1995, A&A, 298, 643
Hou, J., Sánchez, A. G., Scoccimarro, R., et al. 2018, MNRAS, 480, 2521
Ivanov, M. M., & Sibiryakov, S. 2018, JCAP, 07, 053
Ivanov, M. M., Simonović, M., & Zaldarriaga, M. 2020, JCAP, 05, 042
Ivezic, Z., Tyson, J. A., Axelrod, T., et al. 2009, Am. Astron. Soc. Meeting Abstr., 213, 460.03
Jing, Y. P., & Börner, G. 2004, ApJ, 607, 140
Kaiser, N. 1984, ApJ, 284, L9
Landy, S. D., & Szalay, A. S. 1993, ApJ, 412, 64
Laureijs, R., Amiaux, J., Arduini, S., et al. 2011, arXiv e-prints [arXiv:1110.3193]
Lazeyras, T., Wagner, C., Baldauf, T., & Schmidt, F. 2016, JCAP, 02, 018
Lippich, M., Sánchez, A. G., Colavincenzo, M., et al. 2019, MNRAS, 482, 1786
Marín, F. 2011, ApJ, 737, 97
Marín, F. A., Blake, C., Poole, G. B., et al. 2013, MNRAS, 432, 2654
Matsubara, T. 2008, Phys. Rev. D, 77, 063530
McBride, C. K., Connolly, A. J., Gardner, J. P., et al. 2011, ApJ, 739, 85
McDonald, P. 2006, Phys. Rev. D, 74, 103512
McDonald, P., & Roy, A. 2009, JCAP, 08, 020
Moresco, M., Marulli, F., Moscardini, L., et al. 2017, A&A, 604, A133
Moresco, M., Veropalumbo, A., Marulli, F., Moscardini, L., & Cimatti, A. 2021, ApJ, 919, 144
Oddo, A., Rizzo, F., Sefusatti, E., Porciani, C., & Monaco, P. 2021, JCAP, 11, 038
Peacock, J. A., Cole, S., Norberg, P., et al. 2001, Nature, 410, 169
Peebles, P. J. E. 1973, ApJ, 185, 413
Percival, W. J., Cole, S., Eisenstein, D. J., et al. 2007, MNRAS, 381, 1053
Pezzotta, A., de la Torre, S., Bel, J., et al. 2017, A&A, 604, A33
Philcox, O. H. E., & Ivanov, M. M. 2022, Phys. Rev. D, 105, 043517
Potter, D., Stadel, J., & Teyssier, R. 2017, Comput. Astrophys. Cosmol., 4, 2
Pozzetti, L., Hirata, C. M., Geach, J. E., et al. 2016, A&A, 590, A3
Pugno, A., Eggemeier, A., Porciani, C., & Kuruvilla, J. 2025, JCAP, 01, 075
Sánchez, A. G., Kazin, E. A., Beutler, F., et al. 2013, MNRAS, 433, 1202
Sánchez, A. G., Scoccimarro, R., Crocce, M., et al. 2017, MNRAS, 464, 1640
Scoccimarro, R. 2000, ApJ, 542, 1
Scoccimarro, R., Couchman, H. M. P., & Frieman, J. A. 1999, ApJ, 517, 531
Scoccimarro, R., Sefusatti, E., & Zaldarriaga, M. 2004, Phys. Rev. D, 69, 103513
Sefusatti, E., Crocce, M., Pueblas, S., & Scoccimarro, R. 2006, Phys. Rev. D, 74, 023522
Senatore, L., & Zaldarriaga, M. 2015, JCAP, 02, 013
Seo, H.-J., & Eisenstein, D. J. 2003, ApJ, 598, 720
Sheth, R. K., Chan, K. C., & Scoccimarro, R. 2013, Phys. Rev. D, 87, 083002
Slepian, Z., & Eisenstein, D. J. 2015, MNRAS, 454, 4142
Slepian, Z., & Eisenstein, D. J. 2017, MNRAS, 469, 2059
Slepian, Z., & Eisenstein, D. J. 2018, MNRAS, 478, 1468
Slepian, Z., Eisenstein, D. J., Brownstein, J. R., et al. 2017, MNRAS, 469, 1738
Slepian, Z., Eisenstein, D. J., Blazek, J. A., et al. 2018, MNRAS, 474, 2109
Smith, R. E. 2009, MNRAS, 400, 851
Smith, R. E., Scoccimarro, R., & Sheth, R. K. 2007, Phys. Rev. D, 75, 063512
Sugiyama, N. S., Saito, S., Beutler, F., & Seo, H.-J. 2021, MNRAS, 501, 2862
Szalay, A. S. 1988, ApJ, 333, 21
Szapudi, I., & Szalay, A. S. 1998, ApJ, 494, L41
Tröster, T., Sánchez, A. G., Asgari, M., et al. 2020, A&A, 633, L10
Umeh, O. 2021, JCAP, 05, 035
Verde, L., Wang, L., Heavens, A. F., & Kamionkowski, M. 2000, MNRAS, 313, 141
Veropalumbo, A., Sáez Casares, I., Branchini, E., et al. 2021, MNRAS, 507, 1184
Veropalumbo, A., Binetti, A., Branchini, E., et al. 2022, JCAP, 09, 033
Vlah, Z., Seljak, U., Yat Chu, M., & Feng, Y. 2016, JCAP, 03, 057
Wang, Y. 2008, Phys. Rev. D, 77, 123525
Wang, Y., Zhao, G.-B., Chuang, C.-H., et al. 2017, MNRAS, 469, 3762
Zhao, G.-B., Wang, Y., Saito, S., et al. 2017, MNRAS, 466, 762

[1] Dipartimento di Fisica e Astronomia, Università di Bologna, Via Gobetti 93/2, 40129 Bologna, Italy
[2] INAF-Osservatorio di Astrofisica e Scienza dello Spazio di Bologna, Via Piero Gobetti 93/3, 40129 Bologna, Italy
[3] INAF-Osservatorio Astronomico di Brera, Via Brera 28, 20122 Milano, Italy
[4] INFN-Sezione di Genova, Via Dodecaneso 33, 16146 Genova, Italy
[5] Dipartimento di Fisica, Università di Genova, Via Dodecaneso 33, 16146 Genova, Italy
[6] Universität Bonn, Argelander-Institut für Astronomie, Auf dem Hügel 71, 53121 Bonn, Germany

[7] INAF-Osservatorio Astronomico di Trieste, Via G. B. Tiepolo 11, 34143 Trieste, Italy
[8] IFPU, Institute for Fundamental Physics of the Universe, via Beirut 2, 34151 Trieste, Italy
[9] INFN, Sezione di Trieste, Via Valerio 2, 34127 Trieste TS, Italy
[10] Institute of Space Sciences (ICE, CSIC), Campus UAB, Carrer de Can Magrans, s/n, 08193 Barcelona, Spain
[11] Laboratoire Univers et Théorie, Observatoire de Paris, Université PSL, Université Paris Cité, CNRS, 92190 Meudon, France
[12] Université Paris-Saclay, Université Paris Cité, CEA, CNRS, AIM, 91191 Gif-sur-Yvette, France
[13] SISSA, International School for Advanced Studies, Via Bonomea 265, 34136 Trieste TS, Italy
[14] Institut d'Estudis Espacials de Catalunya (IEEC), Edifici RDIT, Campus UPC, 08860 Castelldefels, Barcelona, Spain
[15] Aix-Marseille Université, CNRS, CNES, LAM, Marseille, France
[16] Technion Israel Institute of Technology, Israel
[17] Aix-Marseille Université, Université de Toulon, CNRS, CPT, Marseille, France
[18] Dipartimento di Fisica "Aldo Pontremoli", Università degli Studi di Milano, Via Celoria 16, 20133 Milano, Italy
[19] INFN Gruppo Collegato di Parma, Viale delle Scienze 7/A, 43124 Parma, Italy
[20] Dipartimento di Fisica e Astronomia "G. Galilei", Università di Padova, Via Marzolo 8, 35131 Padova, Italy
[21] INFN-Padova, Via Marzolo 8, 35131 Padova, Italy
[22] Laboratoire d'Annecy-le-Vieux de Physique Theorique, CNRS & Universite Savoie Mont Blanc, 9 Chemin de Bellevue, BP 110, Annecy-le-Vieux, 74941 ANNECY Cedex, France
[23] ICSC – Centro Nazionale di Ricerca in High Performance Computing, Big Data e Quantum Computing, Via Magnanelli 2, Bologna, Italy
[24] INAF – Osservatorio Astronomico di Brera, via Emilio Bianchi 46, 23807 Merate, Italy
[25] Max Planck Institute for Extraterrestrial Physics, Giessenbachstr. 1, 85748 Garching, Germany
[26] School of Mathematics and Physics, University of Surrey, Guildford, Surrey GU2 7XH, UK
[27] Centre National d'Etudes Spatiales – Centre spatial de Toulouse, 18 avenue Edouard Belin, 31401 Toulouse Cedex 9, France
[28] INFN-Sezione di Bologna, Viale Berti Pichat 6/2, 40127 Bologna, Italy
[29] Department of Physics "E. Pancini", University Federico II, Via Cinthia 6, 80126 Napoli, Italy
[30] INAF-Osservatorio Astronomico di Capodimonte, Via Moiariello 16, 80131 Napoli, Italy
[31] Dipartimento di Fisica, Università degli Studi di Torino, Via P. Giuria 1, 10125 Torino, Italy
[32] INFN-Sezione di Torino, Via P. Giuria 1, 10125 Torino, Italy
[33] INAF-Osservatorio Astrofisico di Torino, Via Osservatorio 20, 10025 Pino Torinese (TO), Italy
[34] European Space Agency/ESTEC, Keplerlaan 1, 2201 AZ Noordwijk, The Netherlands
[35] Institute Lorentz, Leiden University, Niels Bohrweg 2, 2333 CA Leiden, The Netherlands
[36] Leiden Observatory, Leiden University, Einsteinweg 55, 2333 CC Leiden, The Netherlands
[37] INAF-IASF Milano, Via Alfonso Corti 12, 20133 Milano, Italy
[38] INAF-Osservatorio Astronomico di Roma, Via Frascati 33, 00078 Monteporzio Catone, Italy
[39] INFN-Sezione di Roma, Piazzale Aldo Moro, 2 – c/o Dipartimento di Fisica, Edificio G. Marconi 00185 Roma, Italy
[40] Centro de Investigaciones Energéticas, Medioambientales y Tecnológicas (CIEMAT), Avenida Complutense 40, 28040 Madrid, Spain
[41] Port d'Informació Científica, Campus UAB, C. Albareda s/n, 08193 Bellaterra (Barcelona), Spain
[42] INFN section of Naples, Via Cinthia 6, 80126 Napoli, Italy
[43] Institute for Astronomy, University of Hawaii, 2680 Woodlawn Drive, Honolulu, HI 96822, USA
[44] Dipartimento di Fisica e Astronomia "Augusto Righi" – Alma Mater Studiorum Università di Bologna, Viale Berti Pichat 6/2, 40127 Bologna, Italy
[45] Instituto de Astrofísica de Canarias, Vía Láctea, 38205 La Laguna, Tenerife, Spain
[46] Institute for Astronomy, University of Edinburgh, Royal Observatory, Blackford Hill, Edinburgh EH9 3HJ, UK
[47] European Space Agency/ESRIN, Largo Galileo Galilei 1, 00044 Frascati, Roma, Italy
[48] ESAC/ESA, Camino Bajo del Castillo, s/n., Urb. Villafranca del Castillo, 28692 Villanueva de la Cañada, Madrid, Spain
[49] Université Claude Bernard Lyon 1, CNRS/IN2P3, IP2I Lyon, UMR 5822, Villeurbanne F-69100, France
[50] Institut de Ciències del Cosmos (ICCUB), Universitat de Barcelona (IEEC-UB), Martí i Franquès 1, 08028 Barcelona, Spain
[51] Institució Catalana de Recerca i Estudis Avançats (ICREA), Passeig de Lluís Companys 23, 08010 Barcelona, Spain
[52] UCB Lyon 1, CNRS/IN2P3, IUF, IP2I Lyon, 4 rue Enrico Fermi, 69622 Villeurbanne, France
[53] Departamento de Física, Faculdade de Ciências, Universidade de Lisboa, Edifício C8, Campo Grande, PT1749-016 Lisboa, Portugal
[54] Instituto de Astrofísica e Ciências do Espaço, Faculdade de Ciências, Universidade de Lisboa, Campo Grande, 1749-016 Lisboa, Portugal
[55] Department of Astronomy, University of Geneva, ch. d'Ecogia 16, 1290 Versoix, Switzerland
[56] Université Paris-Saclay, CNRS, Institut d'astrophysique spatiale, 91405 Orsay, France
[57] Aix-Marseille Université, CNRS/IN2P3, CPPM, Marseille, France
[58] INAF-Istituto di Astrofisica e Planetologia Spaziali, via del Fosso del Cavaliere, 100, 00100 Roma, Italy
[59] Space Science Data Center, Italian Space Agency, via del Politecnico snc, 00133 Roma, Italy
[60] INFN-Bologna, Via Irnerio 46, 40126 Bologna, Italy
[61] School of Physics, HH Wills Physics Laboratory, University of Bristol, Tyndall Avenue, Bristol BS8 1TL, UK
[62] INAF-Osservatorio Astronomico di Padova, Via dell'Osservatorio 5, 35122 Padova, Italy
[63] Universitäts-Sternwarte München, Fakultät für Physik, Ludwig-Maximilians-Universität München, Scheinerstrasse 1, 81679 München, Germany
[64] INFN-Sezione di Milano, Via Celoria 16, 20133 Milano, Italy
[65] Institute of Theoretical Astrophysics, University of Oslo, P.O. Box 1029 Blindern, 0315 Oslo, Norway
[66] Jet Propulsion Laboratory, California Institute of Technology, 4800 Oak Grove Drive, Pasadena, CA 91109, USA
[67] Felix Hormuth Engineering, Goethestr. 17, 69181 Leimen, Germany
[68] Technical University of Denmark, Elektrovej 327, 2800 Kgs. Lyngby, Denmark
[69] Cosmic Dawn Center (DAWN), Denmark
[70] Max-Planck-Institut für Astronomie, Königstuhl 17, 69117 Heidelberg, Germany
[71] NASA Goddard Space Flight Center, Greenbelt, MD 20771, USA
[72] Department of Physics and Astronomy, University College London, Gower Street, London WC1E 6BT, UK
[73] Department of Physics and Helsinki Institute of Physics, Gustaf Hällströmin katu 2, 00014 University of Helsinki, Finland
[74] Université de Genève, Département de Physique Théorique and Centre for Astroparticle Physics, 24 quai Ernest-Ansermet, CH-1211 Genève 4, Switzerland
[75] Department of Physics, P.O. Box 64, 00014 University of Helsinki, Finland
[76] Helsinki Institute of Physics, Gustaf Hällströmin katu 2, University of Helsinki, Helsinki, Finland
[77] Laboratoire d'etude de l'Univers et des phenomenes eXtremes, Observatoire de Paris, Université PSL, Sorbonne Université, CNRS, 92190 Meudon, France

[78] SKA Observatory, Jodrell Bank, Lower Withington, Macclesfield, Cheshire SK11 9FT, UK
[79] Centre de Calcul de l'IN2P3/CNRS, 21 avenue Pierre de Coubertin, 69627 Villeurbanne Cedex, France
[80] University of Applied Sciences and Arts of Northwestern Switzerland, School of Computer Science, 5210 Windisch, Switzerland
[81] Department of Physics, Institute for Computational Cosmology, Durham University, South Road, Durham DH1 3LE, UK
[82] Université Paris Cité, CNRS, Astroparticule et Cosmologie, 75013 Paris, France
[83] CNRS-UCB International Research Laboratory, Centre Pierre Binétruy, IRL2007, CPB-IN2P3, Berkeley, USA
[84] University of Applied Sciences and Arts of Northwestern Switzerland, School of Engineering, 5210 Windisch, Switzerland
[85] Institut d'Astrophysique de Paris, 98bis Boulevard Arago, 75014 Paris, France
[86] Institut d'Astrophysique de Paris, UMR 7095, CNRS, and Sorbonne Université, 98 bis boulevard Arago, 75014 Paris, France
[87] Institute of Physics, Laboratory of Astrophysics, Ecole Polytechnique Fédérale de Lausanne (EPFL), Observatoire de Sauverny, 1290 Versoix, Switzerland
[88] Telespazio UK S.L. for European Space Agency (ESA), Camino bajo del Castillo, s/n, Urbanizacion Villafranca del Castillo, Villanueva de la Cañada, 28692 Madrid, Spain
[89] Institut de Física d'Altes Energies (IFAE), The Barcelona Institute of Science and Technology, Campus UAB, 08193 Bellaterra (Barcelona), Spain
[90] DARK, Niels Bohr Institute, University of Copenhagen, Jagtvej 155, 2200 Copenhagen, Denmark
[91] Waterloo Centre for Astrophysics, University of Waterloo, Waterloo, Ontario N2L 3G1, Canada
[92] Department of Physics and Astronomy, University of Waterloo, Waterloo, Ontario N2L 3G1, Canada
[93] Perimeter Institute for Theoretical Physics, Waterloo, Ontario N2L 2Y5, Canada
[94] Institute of Space Science, Str. Atomistilor, nr. 409 Măgurele, Ilfov 077125, Romania
[95] Consejo Superior de Investigaciones Cientificas, Calle Serrano 117, 28006 Madrid, Spain
[96] Universidad de La Laguna, Departamento de Astrofísica, 38206 La Laguna, Tenerife, Spain
[97] Institut für Theoretische Physik, University of Heidelberg, Philosophenweg 16, 69120 Heidelberg, Germany
[98] Institut de Recherche en Astrophysique et Planétologie (IRAP), Université de Toulouse, CNRS, UPS, CNES, 14 Av. Edouard Belin, 31400 Toulouse, France
[99] Université St Joseph; Faculty of Sciences, Beirut, Lebanon
[100] Departamento de Física, FCFM, Universidad de Chile, Blanco Encalada 2008, Santiago, Chile
[101] Universität Innsbruck, Institut für Astro- und Teilchenphysik, Technikerstr. 25/8, 6020 Innsbruck, Austria
[102] Satlantis, University Science Park, Sede Bld 48940, Leioa-Bilbao, Spain
[103] Department of Physics, Royal Holloway, University of London, TW20 0EX UK
[104] Instituto de Astrofísica e Ciências do Espaço, Faculdade de Ciências, Universidade de Lisboa, Tapada da Ajuda 1349-018, Lisboa, Portugal
[105] Cosmic Dawn Center (DAWN)
[106] Niels Bohr Institute, University of Copenhagen, Jagtvej 128, 2200 Copenhagen, Denmark
[107] Universidad Politécnica de Cartagena, Departamento de Electrónica y Tecnología de Computadoras, Plaza del Hospital 1, 30202 Cartagena, Spain
[108] Centre for Information Technology, University of Groningen, P.O. Box 11044, 9700, CA Groningen, The Netherlands
[109] Kapteyn Astronomical Institute, University of Groningen, PO Box 800, 9700, AV Groningen, The Netherlands
[110] Infrared Processing and Analysis Center, California Institute of Technology, Pasadena, CA 91125, USA
[111] Dipartimento di Fisica e Scienze della Terra, Università degli Studi di Ferrara, Via Giuseppe Saragat 1, 44122 Ferrara, Italy
[112] Istituto Nazionale di Fisica Nucleare, Sezione di Ferrara, Via Giuseppe Saragat 1, 44122 Ferrara, Italy
[113] INAF, Istituto di Radioastronomia, Via Piero Gobetti 101, 40129 Bologna, Italy
[114] Astronomical Observatory of the Autonomous Region of the Aosta Valley (OAVdA), Loc. Lignan 39, I-11020 Nus (Aosta Valley), Italy
[115] Université Côte d'Azur, Observatoire de la Côte d'Azur, CNRS, Laboratoire Lagrange, Bd de l'Observatoire, CS 34229, 06304 Nice cedex 4, France
[116] Department of Physics, Oxford University, Keble Road, Oxford OX1 3RH, UK
[117] Aurora Technology for European Space Agency (ESA), Camino bajo del Castillo, s/n, Urbanizacion Villafranca del Castillo, Villanueva de la Cañada, 28692 Madrid, Spain
[118] Zentrum für Astronomie, Universität Heidelberg, Philosophenweg 12, 69120 Heidelberg, Germany
[119] Department of Mathematics and Physics E. De Giorgi, University of Salento, Via per Arnesano, CP-I93, 73100 Lecce, Italy
[120] INFN, Sezione di Lecce, Via per Arnesano, CP-193, 73100 Lecce, Italy
[121] INAF-Sezione di Lecce, c/o Dipartimento Matematica e Fisica, Via per Arnesano, 73100 Lecce, Italy
[122] INAF-Osservatorio Astronomico di Brera, Via Brera 28, 20122 Milano, Italy, and INFN-Sezione di Genova, Via Dodecaneso 33, 16146 Genova, Italy
[123] ICL, Junia, Université Catholique de Lille, LITL, 59000 Lille, France
[124] Instituto de Física Teórica UAM-CSIC, Campus de Cantoblanco, 28049 Madrid, Spain
[125] CERCA/ISO, Department of Physics, Case Western Reserve University, 10900 Euclid Avenue, Cleveland, OH 44106, USA
[126] Technical University of Munich, TUM School of Natural Sciences, Physics Department, James-Franck-Str. 1, 85748 Garching, Germany
[127] Max-Planck-Institut für Astrophysik, Karl-Schwarzschild-Str. 1, 85748 Garching, Germany
[128] Departamento de Física Fundamental. Universidad de Salamanca, Plaza de la Merced s/n., 37008 Salamanca, Spain
[129] Instituto de Astrofísica de Canarias (IAC); Departamento de Astrofísica, Universidad de La Laguna (ULL), 38200 La Laguna, Tenerife, Spain
[130] Université de Strasbourg, CNRS, Observatoire astronomique de Strasbourg, UMR 7550, 67000 Strasbourg, France
[131] Center for Data-Driven Discovery, Kavli IPMU (WPI), UTIAS, The University of Tokyo, Kashiwa, Chiba 277-8583, Japan
[132] Ludwig-Maximilians-University, Schellingstrasse 4, 80799 Munich, Germany
[133] Max-Planck-Institut für Physik, Boltzmannstr. 8, 85748 Garching, Germany
[134] Dipartimento di Fisica – Sezione di Astronomia, Università di Trieste, Via Tiepolo 11, 34131 Trieste, Italy
[135] Jodrell Bank Centre for Astrophysics, Department of Physics and Astronomy, University of Manchester, Oxford Road, Manchester M13 9PL, UK
[136] California Institute of Technology, 1200 E California Blvd, Pasadena, CA 91125, USA
[137] Department of Physics & Astronomy, University of California Irvine, Irvine, CA 92697, USA
[138] Departamento Física Aplicada, Universidad Politécnica de Cartagena, Campus Muralla del Mar, 30202 Cartagena, Murcia, Spain
[139] Instituto de Física de Cantabria, Edificio Juan Jordá, Avenida de los Castros, 39005 Santander, Spain
[140] Observatorio Nacional, Rua General Jose Cristino, 77-Bairro Imperial de Sao Cristovao, Rio de Janeiro 20921-400, Brazil
[141] CEA Saclay, DFR/IRFU, Service d'Astrophysique, Bat. 709, 91191 Gif-sur-Yvette, France

[142] Institute of Cosmology and Gravitation, University of Portsmouth, Portsmouth PO1 3FX, UK
[143] Department of Computer Science, Aalto University, PO Box 15400, Espoo FI-00 076, Finland
[144] Instituto de Astrofísica de Canarias, c/ Via Lactea s/n, La Laguna 38200, Spain. Departamento de Astrofísica de la Universidad de La Laguna, Avda. Francisco Sanchez, La Laguna 38200, Spain
[145] Ruhr University Bochum, Faculty of Physics and Astronomy, Astronomical Institute (AIRUB), German Centre for Cosmological Lensing (GCCL), 44780 Bochum, Germany
[146] Department of Physics and Astronomy, Vesilinnantie 5, 20014 University of Turku, Finland
[147] Serco for European Space Agency (ESA), Camino bajo del Castillo, s/n, Urbanizacion Villafranca del Castillo, Villanueva de la Cañada, 28692 Madrid, Spain
[148] ARC Centre of Excellence for Dark Matter Particle Physics, Melbourne, Australia
[149] Centre for Astrophysics & Supercomputing, Swinburne University of Technology, Hawthorn, Victoria 3122, Australia
[150] Department of Physics and Astronomy, University of the Western Cape, Bellville, Cape Town 7535, South Africa
[151] DAMTP, Centre for Mathematical Sciences, Wilberforce Road, Cambridge CB3 0WA, UK
[152] Kavli Institute for Cosmology Cambridge, Madingley Road, Cambridge CB3 0HA, UK
[153] Department of Astrophysics, University of Zurich, Winterthurerstrasse 190, 8057 Zurich, Switzerland
[154] Department of Physics, Centre for Extragalactic Astronomy, Durham University, South Road, Durham DH1 3LE, UK
[155] Institute for Theoretical Particle Physics and Cosmology (TTK), RWTH Aachen University, 52056 Aachen, Germany
[156] IRFU, CEA, Université Paris-Saclay, 91191 Gif-sur-Yvette Cedex, France
[157] Oskar Klein Centre for Cosmoparticle Physics, Department of Physics, Stockholm University, Stockholm SE-106 91, Sweden
[158] Astrophysics Group, Blackett Laboratory, Imperial College London, London SW7 2AZ, UK
[159] Univ. Grenoble Alpes, CNRS, Grenoble INP, LPSC-IN2P3, 53, Avenue des Martyrs, 38000 Grenoble, France
[160] INAF-Osservatorio Astrofisico di Arcetri, Largo E. Fermi 5, 50125 Firenze, Italy
[161] Dipartimento di Fisica, Sapienza Università di Roma, Piazzale Aldo Moro 2, 00185 Roma, Italy
[162] Centro de Astrofísica da Universidade do Porto, Rua das Estrelas, 4150-762 Porto, Portugal
[163] Instituto de Astrofísica e Ciências do Espaço, Universidade do Porto, CAUP, Rua das Estrelas, PT4150-762 Porto, Portugal
[164] HE Space for European Space Agency (ESA), Camino bajo del Castillo, s/n, Urbanizacion Villafranca del Castillo, Villanueva de la Cañada, 28692 Madrid, Spain
[165] Theoretical astrophysics, Department of Physics and Astronomy, Uppsala University, Box 516, 751 37 Uppsala, Sweden
[166] Mathematical Institute, University of Leiden, Einsteinweg 55, 2333, CA Leiden, The Netherlands
[167] Institute of Astronomy, University of Cambridge, Madingley Road, Cambridge CB3 0HA, UK
[168] Univ. Lille, CNRS, Centrale Lille, UMR 9189 CRIStAL, 59000 Lille, France
[169] Department of Astrophysical Sciences, Peyton Hall, Princeton University, Princeton, NJ 08544, USA
[170] Space physics and astronomy research unit, University of Oulu, Pentti Kaiteran katu 1, FI-90014 Oulu, Finland
[171] Institut de Physique Théorique, CEA, CNRS, Université Paris-Saclay, 91191 Gif-sur-Yvette Cedex, France
[172] Center for Computational Astrophysics, Flatiron Institute, 162 5th Avenue, 10010 New York, NY, USA

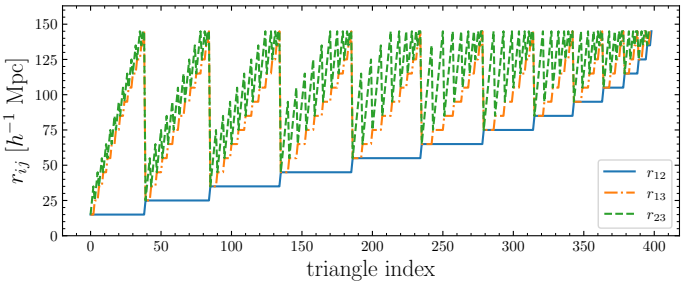

Fig. A.1. Triangle sides (r_{ij}) as a function of the triangle index, following the condition $r_{12} \leq r_{13} \leq r_{23}$.

Appendix A: Dataset

In Fig. A.1 we illustrate how the triangle sides, r_{ij}, vary as a function of the triangle index, with each side shown with dashed lines of different colours.

In Fig. A.2 we show the cumulative signal-to-noise ratio (S/N) for the two statistics as a function of the minimal separation $r_{\rm min}$ computed using the expressions above for the covariance and the $\hat{\xi}$ and $\hat{\zeta}$ measurements as

$$\left(\frac{\rm S}{\rm N}\right)^2_{\xi} := \sum_{r,r'\geq r_{\rm min}} \hat{\xi}(r)\, C^{-1}_{\xi}(r,r')\, \hat{\xi}(r') \tag{A.1}$$

and

$$\left(\frac{\rm S}{\rm N}\right)^2_{\zeta} := \sum_{r_{\rm ij},r'_{\rm ij}\geq r_{\rm min}} \hat{\zeta}(t)\, C^{-1}_{\zeta}(t,t')\, \hat{\zeta}(t'), \tag{A.2}$$

with t and t' corresponding respectively to the triplets $\{r_{12}, r_{13}, r_{23}\}$ and $\{r'_{12}, r'_{13}, r'_{23}\}$. The S/N for the 2PCF is, as might be expected, higher than the 3PCF, but only slightly, and less so at lower redshifts. The two indeed become comparable at mildly non-linear scales. We notice as well that the total signal for the subset of 3PCF configurations defined by $\eta_{\rm min} = 2$ can (see Eq. 40) be larger by a factor of a few with respect to the subset defined by $\eta_{\rm min} = 2$, and, again, it increases at low z.

Appendix B: 2PCF and 3PCF emulators

As detailed in Sect. 5, to efficiently sample the likelihood function as across the three cosmological parameters, we developed an emulator to obtain model predictions rapidly and accurately, in the first place, for the 3PCF, but also extending it to include the 2PCF. Indeed, the computational cost of the predictions for the coefficients ζ_ℓ via Eq. (12) as well as the loop integrals coupled to the Hankel transform of Eq. (5) for the 2PCF makes it impractical to explore a broad range of cosmological parameters directly.

To address this issue, we constructed an emulator implemented in `PyTorch`[4]. The neural network, whose architecture is described in Table B.1, was trained using input samples drawn from a Latin hypercube sampling of the 3D, cosmological parameter space. This spans the ranges $10^9 A_{\rm s} \in [1.045, 3.135]$, $h \in [0.63, 0.73]$, and $\omega_{\rm cdm} \in [0.09, 0.15]$. The full models of both 2PCF and 3PCF can be written as sums of contributions each factorising the dependence on bias and nuisance parameters. This means that we can keep the analytical dependence on these parameters emulating the cosmology-dependence of each individual contribution. The emulator's predictions were subsequently validated against a test set drawn from an independent sample to ensure their accuracy and reliability.

Table B.1. Neural network architecture of the emulator.

Hyperparameter	Value
Number of layers	3
Number of neurons	64
Batch size	256
Learning rate	10^{-3}
Patience value	30
Maximum epochs	300
Validation split	20%
Optimizer	Adam

Notes. The table lists the main hyperparameters adopted in the neural network training, including the number of layers, neurons per layer, and optimisation settings.

The metric chosen for assessing the emulator's performance compares the systematic error $\Delta\xi$ on each separation bin for which $r \geq 7.5\,h^{-1}$Mpc for the 2PCF and $\Delta\zeta$ on each triangular configuration for the 3PCF to their statistical error estimated from the covariance computed in Sect. 4 and with the binning choice adopted there. The statistical error is therefore relative to an observed volume of about $54\,h^{-3}$ Gpc^3, larger than any redshift bin expected for the *Euclid* spectroscopic sample (Euclid Collaboration: Blanchard et al. 2020). In particular, we required that the ratios $\Delta\xi/\sigma_\xi$ and $\Delta\zeta/\sigma_\zeta$ stayed, on average, below the 10% level. The distribution of this metric depends on both the separation (r) and the triangle configuration under consideration, the bias contributions, as well as on the sampled values of the cosmological parameters. This is illustrated by the normalised histograms shown in Fig. B.1. In this test, involving the full model predictions, we assumed a unitary linear bias b_1 and c_0, the bias relations presented in Eqs. (16) and (17), and the fitting function for $b_2(b_1)$ obtained from numerical simulations in Lazeyras et al. (2016). All distributions, for both 2PCF and 3PCF at all four redshifts, are characterised by a median value for $\Delta\xi/\sigma_\xi$ or $\Delta\zeta/\sigma_\zeta$ well below 10%, decreasing slightly with redshift.

This assessment ensures that the emulation process for both the 2PCF and the 3PCF is sufficiently accurate for the analysis presented in this work, but, in practice, also for a direct application to *Euclid* data or measurements from Stage IV surveys. We estimated a possible effect of systematic errors in the emulated prediction by adding in quadrature the mean value of $\Delta\xi$ and $\Delta\zeta$ to the diagonal of the two covariance matrices finding no appreciable difference.

Finally, we notice that the emulator reduces the computational time required for the 3PCF evaluation from approximately 5 minutes per cosmological model to the order of 10^{-3} seconds.

Appendix C: Cosmological constraints

As a complement to the left panel of Fig. 6, in the in the top right, top left and bottom left panels of Fig. C.1 we present here the corresponding results at higher redshifts, namely $z = 1.2$, 1.5, and 1.8. We find that the same qualitative conclusions drawn at $z = 0.9$ continue to hold across redshift, with a general improvement in the precision of parameter inference at lower redshifts. A mild bias in the inferred values of A_s and b_1 is observed, though

[4] https://pytorch.org/docs/stable/index.html

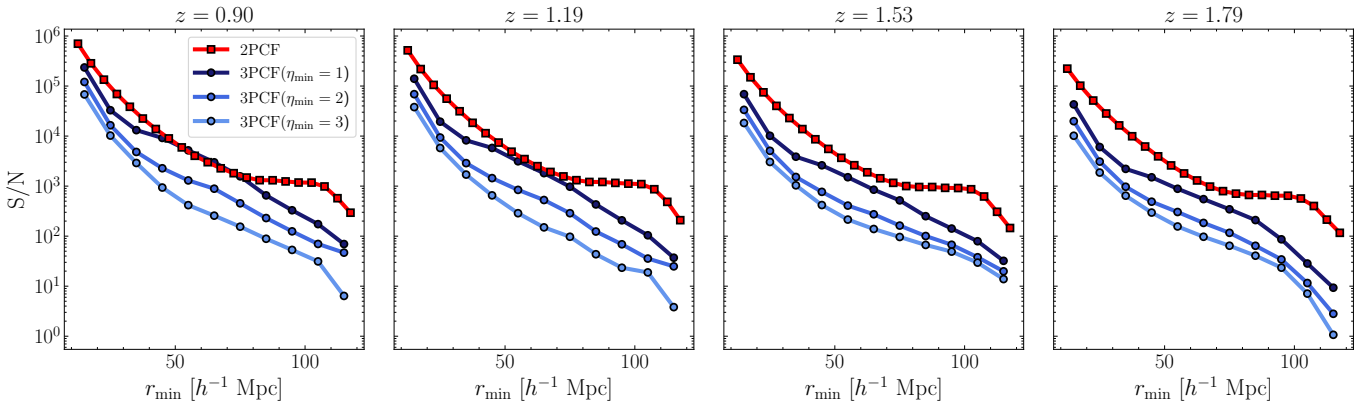

Fig. A.2. Cumulative S/N for the 2PCF and 3PCF measurements computed with the predicted Gaussian covariance according to Eqs. (A.1) and (A.2), as a function of the minimal scale included, $r_{\rm min}$.

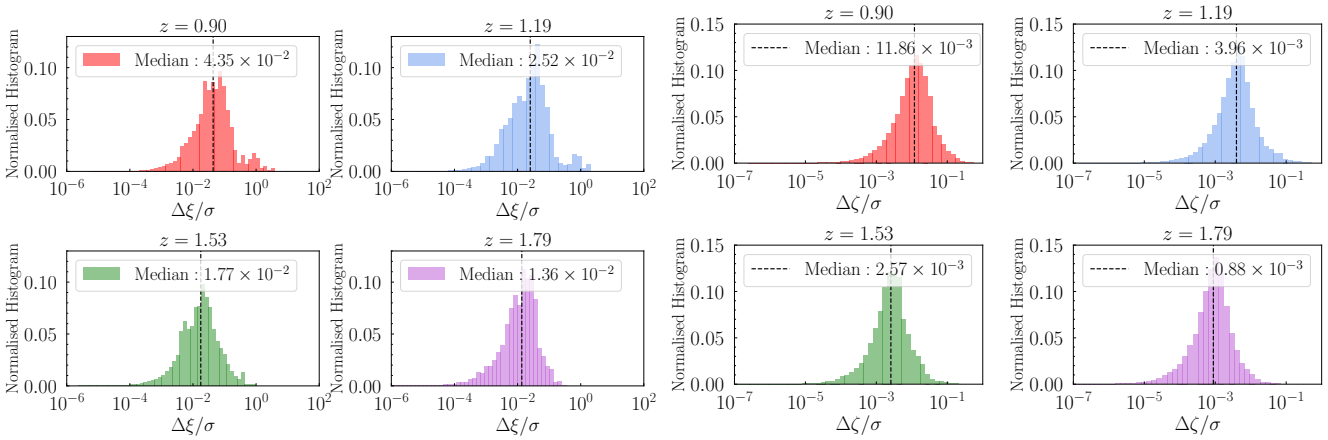

Fig. B.1. Normalised histogram of the ratio between the difference between emulated and exact modelling 2PCF predictions and the corresponding uncertainty, Δ_ξ/σ_ξ (top four panels). Different colours refer to different redshift snapshot, while the dashed black line represents the median of the distribution. The same quantity for the 3PCF, $\Delta_\zeta/\sigma_\zeta$, is shown in the bottom four panels, for the different redshifts.

still well within statistical compatibility with the expected values. We interpret this as a residual effect of projection, and note that all snapshots share the same seed. Moreover, we combined all redshift snapshots to derive constraints on the cosmological parameters $A_s, \omega_{\rm cdm}, h$, as shown in bottom right panel Fig. C.1. In this combined analysis, we treated the cosmological parameters as shared across all redshifts while allowing the bias parameters to vary independently for each redshift bin, reflecting the expected evolution of galaxy bias with redshift. The combined constraints show significant improvement in precision compared to individual redshift analyses, demonstrating the enhanced constraining power achievable by combining multiple redshifts snapshots. We note that these snapshots are correlated as they share the same simulation seed, which should be taken into account when interpreting the statistical significance of the improvement.

Finally, in Fig C.2 we show the full extension of the right panel of Fig. 6, including all model parameters and, in particular, the non-linear galaxy bias terms, $b_2, b_{\mathcal{G}_\epsilon}$, and b_{Γ_3}, and the EFT parameters, c_0. This figure also illustrates how the impact of consistency relations on the bias parameter constraints becomes increasingly important as cosmological parameters are marginalised over, with the strongest effects visible for the degeneracy between A_s and b_1. This highlights the critical role of consistency relations in enabling accurate cosmological inference once the cosmological parameter space is opened.

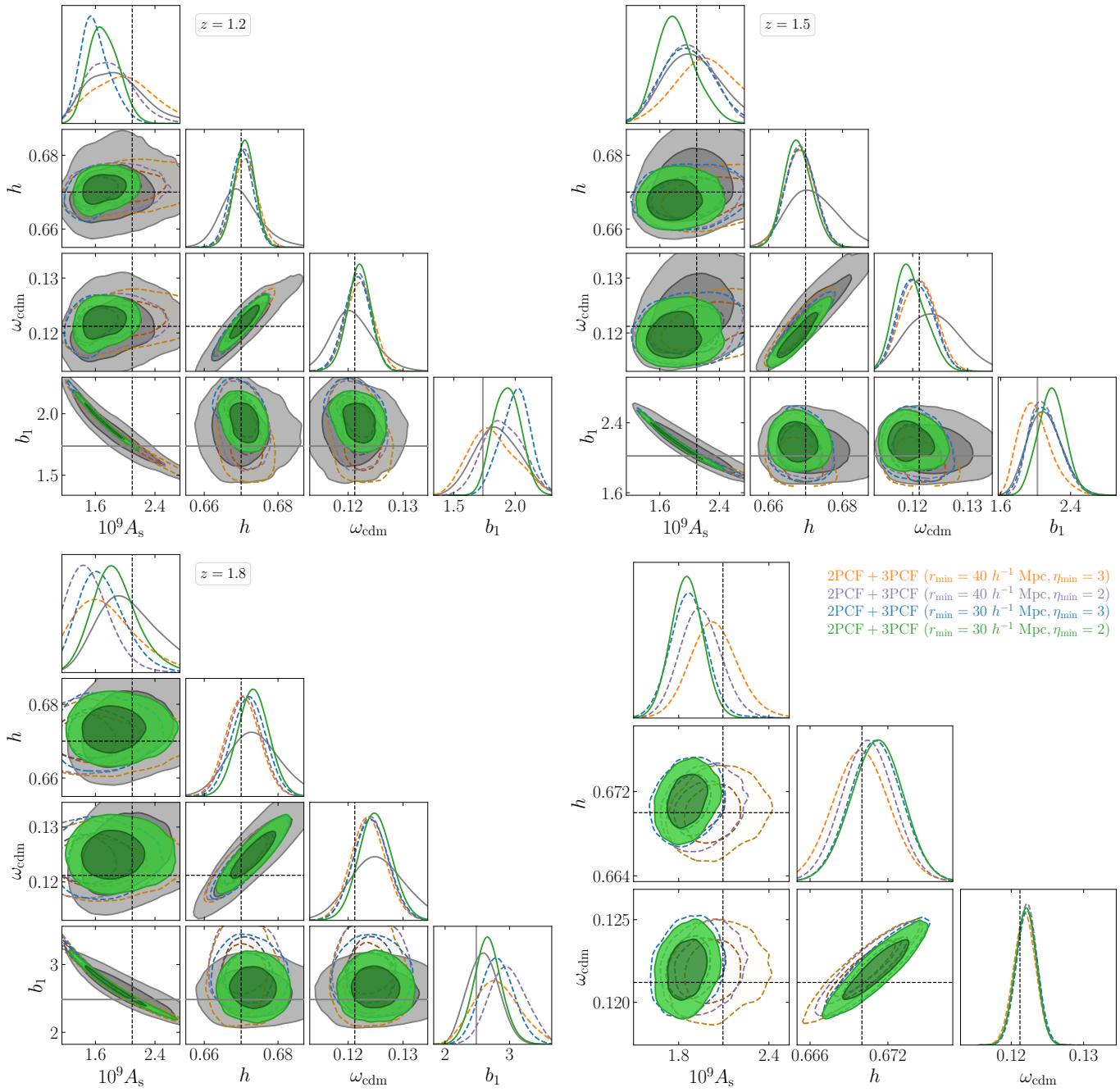

Fig. C.1. *Top right, top left,* and *bottom left:* Joint 2PCF+3PCF cosmological constraints and the linear bias b_1 for individual redshift snapshots at $z = 1.2$, $z = 1.5$, and $z = 1.8$, following the format of Fig. 6. *Bottom right*: Combined cosmological constraints from all redshift bins ($z = 0.9, 1.2, 1.5$, and 1.8).

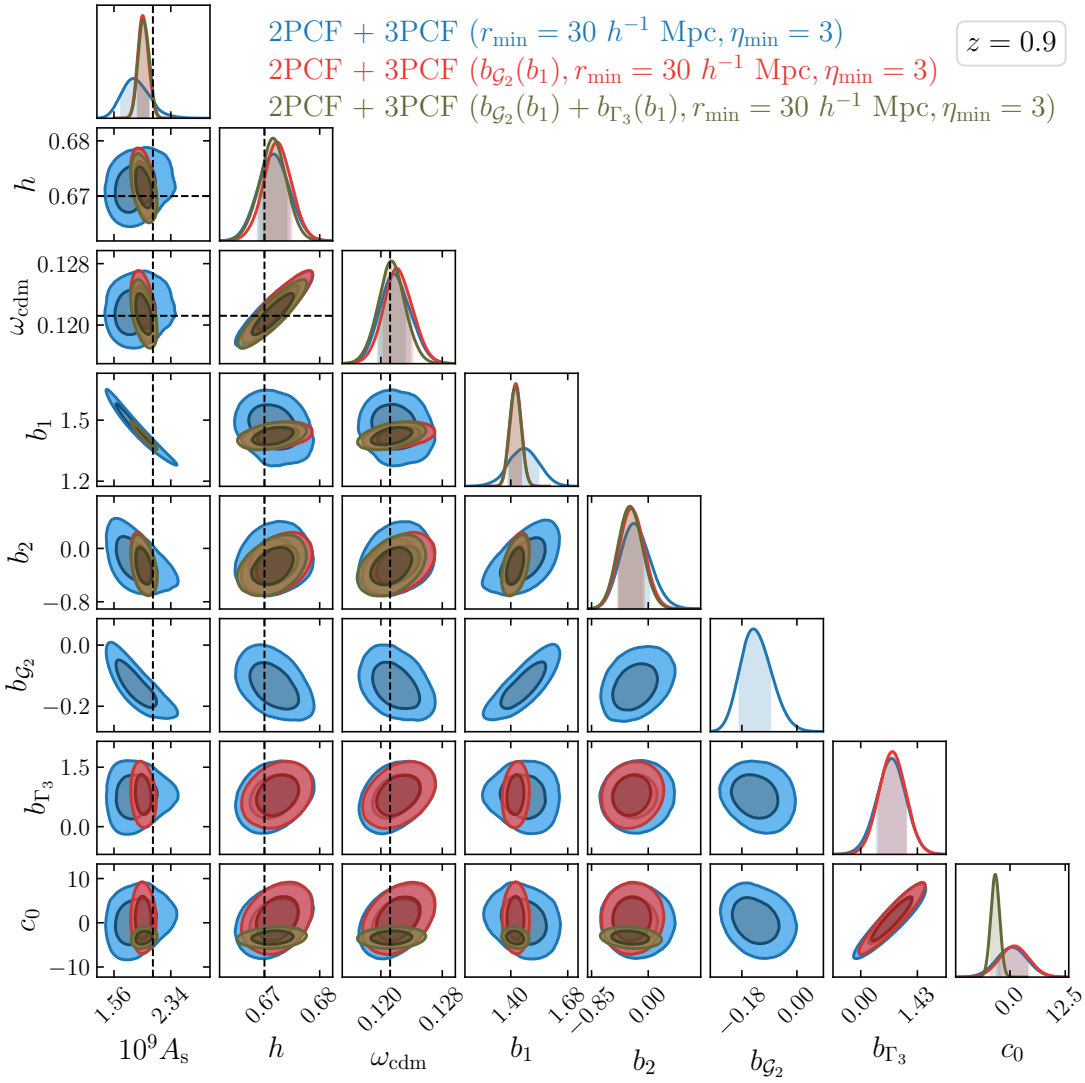

Fig. C.2. Same as the right panel of Fig. 6 but showing the full set of model parameters.